

## THE SPIN-DOWN OF PSR J0821–4300 AND PSR J1210–5226: CONFIRMATION OF CENTRAL COMPACT OBJECTS AS ANTI-MAGNETARS

E. V. GOTTHELF, J. P. HALPERN, AND J. ALFORD

Columbia Astrophysics Laboratory, Columbia University, 550 West 120th Street, New York, NY 10027, USA

Received 2012 September 23; accepted 2013 January 11; published 2013 February 15

### ABSTRACT

Using *XMM-Newton* and *Chandra*, we measure period derivatives for the second and third known pulsars in the class of central compact objects (CCOs) in supernova remnants, proving that these young neutron stars have exceptionally weak dipole magnetic field components. For the 112 ms PSR J0821–4300 in Puppis A,  $\dot{P} = (9.28 \pm 0.36) \times 10^{-18}$ . Its proper motion,  $\mu = 61 \pm 9$  mas yr $^{-1}$ , was also measured using *Chandra*. This contributes a kinematic term to the period derivative via the Shklovskii effect, which is subtracted from  $\dot{P}$  to derive dipole  $B_s = 2.9 \times 10^{10}$  G, a value similar to that of the first measured CCO, PSR J1852+0040 in Kes 79, which has  $B_s = 3.1 \times 10^{10}$  G. Antipodal surface hot spots with different temperatures and areas are deduced from the X-ray spectrum and pulse profiles. Paradoxically, such nonuniform surface temperature appears to require strong crustal magnetic fields, probably toroidal or quadrupolar components much stronger than the external dipole. A spectral feature, consisting of either an emission line at  $\approx 0.75$  keV or an absorption line at  $\approx 0.46$  keV, is modulated in strength with the rotation. It may be due to a cyclotron process in a magnetic field on the surface that is slightly stronger than the dipole deduced from the spin-down. We also timed anew the 424 ms PSR J1210–5226, resolving previous ambiguities about its spin-down rate. Its  $\dot{P}$  is  $(2.22 \pm 0.02) \times 10^{-17}$ , corresponding to  $B_s = 9.8 \times 10^{10}$  G. This is also compatible with a cyclotron resonance interpretation of its prominent absorption line at 0.7 keV and its harmonics. These results deepen the mystery of the origin and evolution of CCOs: Why are their numerous descendants not evident?

**Key words:** ISM: individual objects (Puppis A) – pulsars: individual (PSR J0821–4300, PSR J1210–5226, PSR J1852+0040) – stars: neutron

*Online-only material:* color figures

### 1. INTRODUCTION

The class of faint X-ray sources in supernova remnants (SNRs) known as central compact objects (CCOs) are characterized by steady flux, predominantly surface thermal X-ray emission, lack of a surrounding pulsar wind nebula, and absence of detection at any other wavelength. Table 1 lists basic data on the well-studied CCOs, as well as proposed candidates whose qualifications are not yet well established. Of the eight most secure CCOs, three are known to be neutron stars (NSs) with spin periods of 0.105, 0.424, and 0.112 s. Spin-down has been detected for two of these, the 0.105 s pulsar PSR J1852+0040 in Kes 79 and the 0.424 s pulsar PSR J1210–5226 in the SNR PKS 1209–51/52. For PSR J1852+0040, the implied surface dipole field is only  $B_s = 3.1 \times 10^{10}$  G (Halpern & Gotthelf 2010a), smaller than that of any other young known NS. In the case of PSR J1210–5226, archival data allow two alternative timing solutions, with  $B_s = 9.9 \times 10^{10}$  or  $2.4 \times 10^{11}$  G (Halpern & Gotthelf 2011).

It is natural to assume that CCOs that have not yet been seen to pulse are isolated, weakly magnetized NSs of the same class as the CCO pulsars. Where pulsar searches have been unsuccessful, it is possible that an even weaker magnetic field, a more uniform surface temperature, or an unfavorable viewing geometry, prevents detection of rotational modulation. The absence of pulsations from the youngest known NS, the  $\approx 330$  year old CCO in Cassiopeia A, has been used, in combination with fitting of its X-ray spectrum, to argue that it is covered with a uniform temperature, non-magnetized atmosphere of carbon, the product of nuclear burning of H and He (Ho & Heinke 2009). Rapid cooling of the NS in Cas A, directly detected by *Chandra* (Heinke & Ho 2010), has been

interpreted as evidence for neutron superfluidity in the core (Page et al. 2011; Shternin et al. 2011).

The “anti-magnetar” explanation of CCOs, which is motivated by their weak magnetic fields, absence of variability, and location on the  $P$ – $\dot{P}$  diagram, remains incomplete in detail. Specifically, it does not yet account for the hot spots that are seen on the surfaces of CCO pulsars. Since the spin-down power of a CCO pulsar is less than its X-ray luminosity, the latter must be thermal emission from residual cooling, which can only be nonuniform if there is anisotropic heat conduction. In the absence of strong magnetic fields or magnetospheric activity, it is difficult to reproduce the light curve and pulsed fraction of 64% from PSR J1852+0040 in Kes 79 (Halpern & Gotthelf 2010a; Shabaltas & Lai 2012), or the two antipodal hot spots of different temperatures and areas on RX J0822–4300 in Puppis A (Gotthelf & Halpern 2009; Gotthelf et al. 2010). The latter 0.112 s pulsar, hereafter PSR J0821–4300, is a subject of this paper. Its spectrum is especially puzzling in also displaying a phase-dependent emission feature at 0.7–0.8 keV (Gotthelf & Halpern 2009), which is reported to be variable in the long term (De Luca et al. 2012).

Here we report the first spin-down measurement for PSR J0821–4300, based on a dedicated program of phase-coherent timing jointly scheduled between *XMM-Newton* and *Chandra*. It was also necessary to incorporate *Chandra* HRC observations of the position and proper motion of PSR J0821–4300 in order to determine its small period derivative accurately. The astrometric analysis is described in Section 2. (The latter work was also carried out, with consistent results, by Becker et al. 2012.) The results of the timing are presented in Section 3. The X-ray flux and spectra are discussed in Section 4, with particular attention paid to the spectral line and the question of its possible

**Table 1**  
Central Compact Objects in Supernova Remnants

| CCO                     | SNR            | Age<br>(kyr) | $d$<br>(kpc) | $P$<br>(s) | $f_p^a$<br>(%) | $B_s$<br>( $10^{10}$ G) | $L_{x,\text{bol}}$<br>(erg s $^{-1}$ ) | References           |
|-------------------------|----------------|--------------|--------------|------------|----------------|-------------------------|--|----------------------|
| RX J0822.0–4300         | Puppis A       | 4.5          | 2.2          | 0.112      | 11             | 2.9                     | $5.6 \times 10^{33}$                   | 1,2,3,4,5,6          |
| CXOU J085201.4–461753   | G266.1–1.2     | 1            | 1            | ...        | <7             | ...                     | $2.5 \times 10^{32}$                   | 7,8,9,10,11          |
| 1E 1207.4–5209          | PKS 1209–51/52 | 7            | 2.2          | 0.424      | 9              | 9.8                     | $2.5 \times 10^{33}$                   | 6,12,13,14,15,16,17  |
| CXOU J160103.1–513353   | G330.2 + 1.0   | ≥3           | 5            | ...        | <40            | ...                     | $1.5 \times 10^{33}$                   | 18,19                |
| 1WGA J1713.4–3949       | G347.3–0.5     | 1.6          | 1.3          | ...        | <7             | ...                     | $\sim 1 \times 10^{33}$                | 11,20,21             |
| XMMU J172054.5–372652   | G350.1–0.3     | 0.9          | 4.5          | ...        | ...            | ...                     | $3.9 \times 10^{33}$                   | 22,23                |
| CXOU J185238.6 + 004020 | Kes 79         | 7            | 7            | 0.105      | 64             | 3.1                     | $5.3 \times 10^{33}$                   | 24,25,26,27          |
| CXOU J232327.9 + 584842 | Cas A          | 0.33         | 3.4          | ...        | <12            | ...                     | $4.7 \times 10^{33}$                   | 27,28,29,30,31,32,33 |
| 2XMMi J115836.1–623516  | G296.8–0.3     | 10           | 9.6          | ...        | ...            | ...                     | $1.1 \times 10^{33}$                   | 34                   |
| XMMU J173203.3–344518   | G353.6–0.7     | ~27          | 3.2          | ...        | <9             | ...                     | $1.3 \times 10^{34}$                   | 35,36,37,38          |
| CXOU J181852.0–150213   | G15.9 + 0.2    | 1–3          | (8.5)        | ...        | ...            | ...                     | $\sim 1 \times 10^{33}$                | 39                   |

**Notes.** Above the line are eight well-established CCOs. Below the line are three candidates.

<sup>a</sup> Upper limits on pulsed fraction are for a search down to  $P = 12$  ms or smaller.

**References.** (1) Hui & Becker 2006a; (2) Gotthelf & Halpern 2009; (3) Gotthelf et al. 2010; (4) De Luca et al. 2012; (5) Becker et al. 2012; (6) this paper; (7) Slane et al. 2001; (8) Kargaltsev et al. 2002; (9) Bamba et al. 2005; (10) Iyudin et al. 2005; (11) De Luca 2008; (12) Zavlin et al. 2000; (13) Mereghetti et al. 2002a; (14) Bignami et al. 2003; (15) De Luca et al. 2004; (16) Gotthelf & Halpern 2007; (17) Halpern & Gotthelf 2011; (18) Park et al. 2006; (19) Park et al. 2009; (20) Lazendic et al. 2003; (21) Cassam-Chenai et al. 2004; (22) Gaensler et al. 2008; (23) Lovchinsky et al. 2011; (24) Seward et al. 2003; (25) Gotthelf et al. 2005; (26) Halpern et al. 2007; (27) Halpern & Gotthelf 2010a; (28) Pavlov et al. 2000; (29) Chakrabarty et al. 2001; (30) Mereghetti et al. 2002b; (31) Pavlov & Luna 2009; (32) Ho & Heinke 2009; (33) Heinke & Ho 2010; (34) Sánchez-Ayaso et al. 2012; (35) Tian et al. 2008; (36) Abramowski et al. 2011; (37) Halpern & Gotthelf 2010b; (38) Halpern & Gotthelf 2010c; (39) Reynolds et al. 2006.

**Table 2**  
Log of *Chandra* HRC-I Observations of PSR J0821–4300

| ObsID | Date<br>(UT) | Start Epoch<br>(MJD) | Exposure<br>(ks) | Roll Angle<br>(°) | Star A<br>(counts) <sup>a</sup> | PSR J0821–4300<br>(counts) <sup>a</sup> |
|-------|--------------|----------------------|------------------|-------------------|---------------------------------|---|
| 749   | 1999 Dec 21  | 51533.95             | 18.0             | 338.7             | 47                              | 3257                                    |
| 4612  | 2005 Apr 25  | 53485.31             | 40.2             | 261.9             | 123                             | 7260                                    |
| 11819 | 2010 Aug 10  | 55418.72             | 33.7             | 163.4             | 101                             | 5455                                    |
| 12201 | 2010 Aug 11  | 55419.13             | 38.7             | 162.9             | 117                             | 6296                                    |

**Note.** <sup>a</sup> Total counts collected in a 1.5'' radius aperture centered on the source.

variability. We also obtained new timing observations of PSR J1210–5226 that resolve the prior ambiguity about its spin-down rate in favor of the smaller value; this definitive result is presented in Section 5. The nature of CCOs as anti-magnetars, and their possible evolutionary status, are discussed in Section 6. Conclusions and proposals for future work follow in Section 7.

## 2. X-RAY POSITION AND PROPER MOTION

Evidence that PSR J0821–4300 has high proper motion from *Chandra* HRC images over a 5 year baseline was reported by Hui & Becker (2006b) and Winkler & Petre (2007), but with slightly disparate measurements of  $\mu = 107 \pm 34$  mas yr $^{-1}$  and  $\mu = 165 \pm 25$  mas yr $^{-1}$ , respectively, from the same data. Here, we are concerned with timing this high-velocity pulsar over an extended period of time with millisecond accuracy. When trying to measure a small  $\dot{P}$  using X-ray data, position and proper motion can contribute significant errors via three effects. The first is an instrumental property of the *Chandra* CCDs when used in continuous-clocking (CC) mode (see Section 3); the position of the pulsar must be known a priori to  $<0.5''$  in order to determine the time of arrival of each source photon. The second consideration is the accuracy of the barycentric correction. The third effect is the magnitude of the proper motion, which contributes a purely kinematic period derivative via the “train whistle” effect (Shklovskii 1970). The original measurements of proper motion are not accurate enough to measure this effect, which is crucial in the case of PSR J0821–4300.

Accordingly, we have reanalyzed the position and proper motion of PSR J0821–4300 using the *Chandra* HRC-I data listed in Table 2, which now includes a more recent pair of observations in 2010 August that extends the baseline to 10.6 yr, enabling higher precision on both the contemporary position for timing, and the proper motion. We will describe here any differences between our method and previous work. For example, we did not use an HRC-S observation (ObsID 1851) because of known systematic differences between HRC-S and HRC-I. Ultimately, however, our results are consistent with the recent analysis of the same data (including ObsID 1851) by Becker et al. (2012).

The data from all epochs were reprocessed and analyzed using the latest calibration files and software (CIAO 4.4/CALDB 4.4.8). This processing accounts for the HRC AMP\_SF electronic ringing distortions discussed by Hui & Becker (2006b). The HRC detector is well suited to astrometry, with its processed pixel size of 0.1318'' that oversamples the on-axis point-spread function (PSF) by a factor of five. For all observations, the pulsar was placed close to the optical axis where the PSF is essentially symmetric. In the following analysis we assume, as there is no evidence to the contrary, that the HRC focal plane is linear and the aspect reconstruction introduces no errors in roll angle. The two pointings on consecutive days in 2010 August are sufficiently different in their aspect reconstruction that we analyze them individually.

The nominal uncertainty in aspect reconstruction for a typical *Chandra* observation is 0.6''. It is often possible to remove most

of this systematic error by using nearby X-ray point sources with precisely measured optical coordinates to correct the absolute astrometry. Hui & Becker (2006b) used their X-ray detected “star A” as their sole fiducial point, and fitted a model PSF interpolated from the CIAO library appropriate for its position and estimated photon energy to determine its position. Winkler & Petre (2007) used this star and two additional stars, and followed the updated method outlined in the CIAO thread for generating a Monte Carlo PSF using the CHaRT/MARX software for input into the CIAO/Sherpa spectral/image fitting software package.

In our analysis, we also follow the CIAO thread to characterize the HRC-I PSF, but we adopt a simpler approach to measuring source locations, one that is not dependent on model fitting in the image domain. Our method is guided by the following observations. First, the on-axis, symmetric image of the pulsar contains enough counts that a simple centroid calculation is a sufficiently accurate measurement of its position on the detector. Second, star A of Hui & Becker (2006b), which lies  $2.7'$  from PSR J0821–4300, is the only useful fiducial source for registering the X-ray image. The position and proper motion of star A are taken from the UCAC3 (Zacharias et al. 2010), where it is listed as 3UC094-058669 with coordinates (J2000.0) R.A. =  $08^{\text{h}}21^{\text{m}}46\rlap{.}^s2924(16)$ , decl. =  $-43^{\circ}02'03\rlap{.}''640(49)$ , and proper motion  $\mu_{\alpha} \cos \delta = -14.3(2.0)$ ,  $\mu_{\delta} = -3.6(5.5)$  mas yr<sup>-1</sup>. X-ray position measurements of the two weaker, off-axis stars used by Winkler & Petre (2007) only add to the uncertainty (as quantified below) in the absolute astrometry. Third, the few X-ray photons from star A, and its broad off-axis PSF, do not warrant a sophisticated image fitting technique. Instead, we use a “corrected centroid” method, as described below.

To determine the source location of star A in the X-ray images we start with the CHaRT/MARX simulation of the PSF, as described in the CIAO user Web site,<sup>1</sup> for its respective locations on the focal plane. Figure 1 shows the distribution of the counts from each HRC image and corresponding Monte Carlo PSF. It is apparent that star A is poorly sampled in the data, with total source counts in the range  $47 \leq N \leq 123$  (Table 2). The maximum number of counts per pixel is typically only 2–4, making forward fitting poorly constrained statistically, while sharp features in the model can cause systematic offsets. Furthermore, the source is immersed in a substantial diffuse background from the Puppis A SNR, which, although it only contributes a few photons over the source region, adds uncertainty to the position measurement because of the small-count statistics, especially when fitting over a larger area.

To sidestep these effects, the coordinates of star A are first found from its centroid. Photons were extracted from circular aperture of radius  $1''.5$ , chosen to minimize the background counts. This aperture encloses essentially all of the signal in that fraction of the PSF with a finite probability of producing a single count during the observation. This measurement was made using the CIAO tool *dmstat* and is iterated to produce the final coordinates. However, while this results in a well-defined and statistically meaningful measurement, it does not account for the shape of the complex off-axis PSF, whose orientation depends on the spacecraft roll angle (which differs for each observation; see Figure 1), or for the monotonic off-axis deviations introduced by the flat focal plane. To quantify these systematic effects we also measure the centroid of the simulated PSF of star A in sky coordinates in each image and compare it

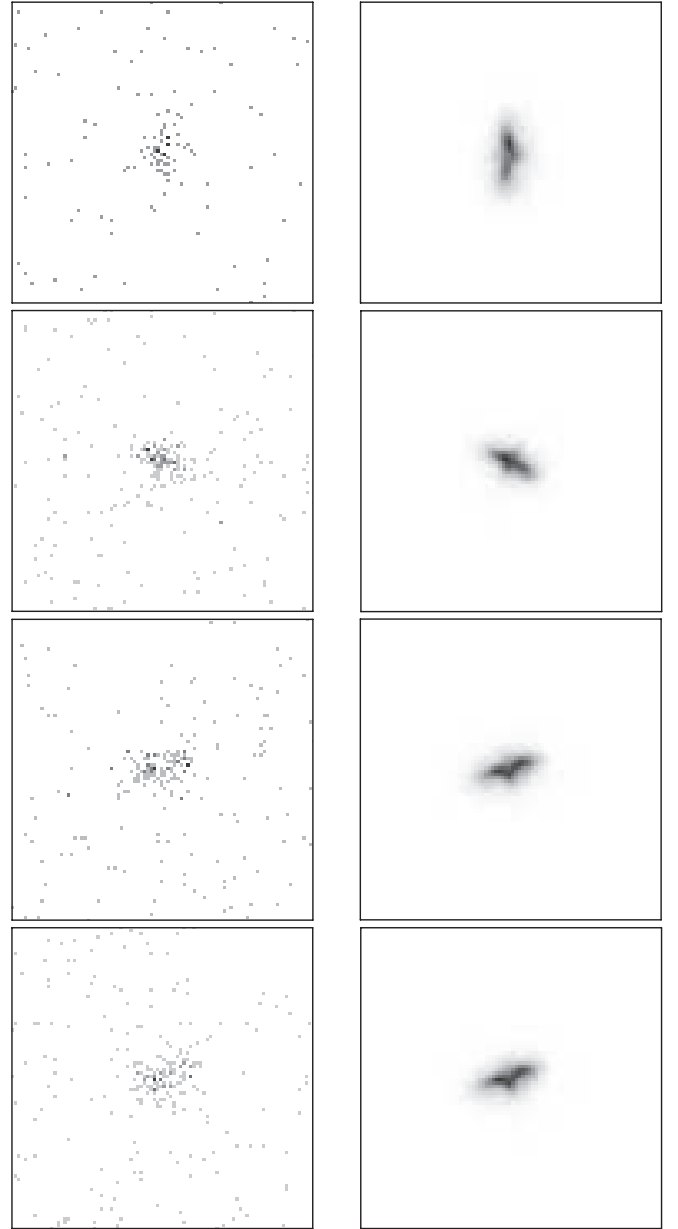


**Figure 1.** *Chandra* HRC-I images around reference star A (3UC094-058669) used to define the coordinate system for position and proper motion of PSR J0821–4300. Each panel shows the observed counts from Star A (left) and the simulated PSF (right) for its location on the focal plane in native HRC-I pixels. The plots cover  $12'' \times 12''$  in celestial coordinates. The total counts in a  $1''.5$  radius aperture are given in Table 3. From top to bottom, the dates of the observations are given in Table 2.

to the coordinates that were input to CHaRT/MARX for that PSF. The difference constitutes the small, but critical correction to the centroid of star A.

We estimated the uncertainty in the derived coordinates of star A using a Monte Carlo method. We generated 500 realizations of star A by sampling the PSF using a random number generator to match the observed counts, and accumulated the centroid measurements to build up a distribution in right ascension and declination. To account for the observed background, we included a random distribution of photons within the source aperture. The resulting (Gaussian) width of the distribution of centroids is typically  $\sigma \approx 0''.06$  in each of the two coordinates (see Table 3). These reproduce the expected “standard error”

<sup>1</sup> <http://cxc.harvard.edu/chart>

**Table 3**  
Position Measurements for PSR J0821–4300

| Epoch<br>(yr) | Star A (Optical)  |                          | Star A (X-Ray)    |                          | PSR J0821–4300 (Corrected) |                          |
|---------------|-------------------|--------------------------|-------------------|--------------------------|----------------------------|--------------------------|
|               | R.A. (h m s)      | Decl. ( $^{\circ} '$ '') | R.A. (h m s)      | Decl. ( $^{\circ} '$ '') | R.A. (h m s)               | Decl. ( $^{\circ} '$ '') |
| 1999.975      | 08 21 46.2928(16) | -43 02 03.637(49)        | 08 21 46.2882(65) | -43 02 03.397(83)        | 08 21 57.4024(67)          | -43 00 16.894(96)        |
| 2005.316      | 08 21 46.2858(21) | -43 02 03.657(57)        | 08 21 46.3011(47) | -43 02 03.756(41)        | 08 21 57.3685(52)          | -43 00 17.023(71)        |
| 2010.610      | 08 21 46.2789(31) | -43 02 03.676(76)        | 08 21 46.2621(62) | -43 02 04.113(47)        | 08 21 57.3488(69)          | -43 00 17.185(89)        |
| 2010.611      | 08 21 46.2789(31) | -43 02 03.676(76)        | 08 21 46.2575(57) | -43 02 04.068(51)        | 08 21 57.3476(65)          | -43 00 17.190(92)        |

**Notes.** All coordinates are equinox J2000. Optical coordinates for star A (3UC094-058669) are corrected for the epoch of proper motion. The X-ray position of star A is determined using the method described in the text. The pulsar coordinates are corrected by the difference between the optical and X-ray coordinates of star A. Uncertainties on the last digits are in parentheses.

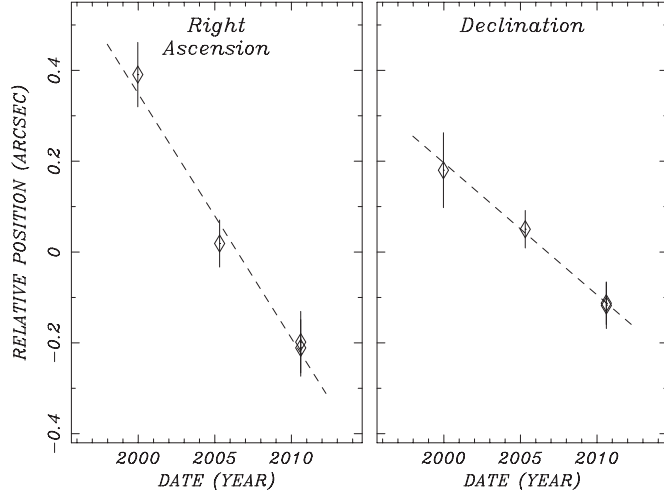


**Figure 2.** Four position measurements of PSR J0821–4300 spanning 10.6 yr, after correction using the optical/X-ray star A (3UC094-058669) as a reference. The two observations in 2010 nearly coincide in time. The positions (diamonds) and their errors are fitted with a linear model (dashed lines). The fitted parameters are listed in Table 5.

for a centroid,  $\approx\sigma/\sqrt{N}$ . We also simulated the uncertainties for the two other fiducial sources used in Winkler & Petre (2007) and find that their inclusion in the position determination would only increase the uncertainty on the final coordinates.

The pulsar itself is a strong source (see Table 2) whose coordinates are precisely measured using a centroid calculation with uncertainty an order of magnitude smaller than those measured for star A. Because of the symmetry of its on-axis PSF, no systematic correction is required for the pulsar. Its coordinates are then adjusted by the difference between the optical and X-ray coordinates of star A at each epoch to produce its final astrometric position in Table 3. Fitting the position of the pulsar as a function of time then yields the proper motion. Figure 2 shows the  $\chi^2$  fit with constant velocity in each coordinate, and Table 5 lists the formal solution and quantities derived from it. The derived total proper motion of  $61 \pm 9$  mas yr $^{-1}$  is in agreement with the value determined by Becker et al. (2012),  $71 \pm 12$  mas yr $^{-1}$ , and is smaller than previously published numbers for reasons discussed in that paper.

The tangential velocity of PSR J0821–4300 then depends on a distance determination for Puppis A, which has ranged from 1 to 2.5 kpc according to various methods, and is a matter of unresolved debate in the most recent studies quoted here. One (Reynoso et al. 1995, 2003) is based on 21 cm H $\alpha$  velocities, and a perceived morphological association of features in H $\alpha$

surrounding the pulsar and the SNR at  $v_{\text{lsr}} = +16$  km s $^{-1}$ , the latter corresponding to  $d = 2.2 \pm 0.3$  kpc. The second method uses spectra of ground-state hydroxyl lines (Woermann et al. 2000), which show absorption at  $v_{\text{lsr}} < +7.6$  km s $^{-1}$ , and emission above this velocity, from which  $d = 1.3^{+0.6}_{-0.8}$  kpc is derived. Both sets of authors employ assumptions that are not mutually accepted, and are beyond the scope of this paper to evaluate. We will adopt a fiducial distance of  $2.2 \pm 0.3$  kpc for purposes of further calculations, while noting the implications of a possible smaller distance where relevant.

The tangential velocity of PSR J0821–4300 at  $d = 2.2 \pm 0.3$  kpc is  $v_{\perp} = 636 \pm 126$  km s $^{-1}$ . This velocity is at the high end of the distribution of two-dimensional velocities of pulsars measured by Hobbs et al. (2005), who find mean values of  $\bar{v}_{\perp} = 246 \pm 22$  km s $^{-1}$  for 121 ordinary (non-recycled) pulsars, and  $\bar{v}_{\perp} = 307 \pm 47$  km s $^{-1}$  for 46 pulsars whose characteristic ages are  $<3$  Myr. The individual pulsar velocities are corrected for the solar motion with respect to the local standard of rest and a flat Galactic rotation curve in order to express them in the frame of the rotating Galactic disk. In the case of PSR J0821–4300 this correction is dominated by the solar motion for the range of plausible distances, and is only  $-7$  km s $^{-1}$ , resulting in a corrected tangential velocity of  $v_{\perp,c} = 629$  km s $^{-1}$ . If the distance is as small as 1 kpc, this reduces to an unexceptional 290 km s $^{-1}$ .

The Shklovskii (1970) effect, a purely kinematic contribution to the observed period derivative, will be significant. For a source moving at constant velocity the kinematic contribution is

$$\dot{P}_k = \frac{\mu^2 P d}{c} = \frac{v_{\perp}^2 P}{d c}. \quad (1)$$

From the proper-motion measurement of PSR J0821–4300,  $\dot{P}_k = (2.24 \pm 0.72) \times 10^{-18}$  is calculated, where we have propagated the uncertainties on both  $\mu$  and  $d$ .

### 3. X-RAY TIMING

Previous observations of PSR J0821–4300 were only able to set upper limits on its period derivative (Gotthelf & Halpern 2009; Gotthelf et al. 2010; De Luca et al. 2012). Evidently  $\dot{P}$  is so small that it can only be measured by phase-coherent timing. Accordingly, we designed a sequence of observations coordinated between *XMM-Newton* and *Chandra* that would start and maintain phase connection over a 2 year span, 2010 May to 2012 April. The scheduling strategy is the same as was used for PSR J1852 + 0040 in Kes 79 (Halpern & Gotthelf 2010a). By design, the resulting ephemeris was also connected backward to archival observations that were obtained in 2009 December and 2010 April (De Luca et al. 2012), which extended

**Table 4**  
Log of X-Ray Timing Observations of PSR J0821–4300

| Mission | Instr/Mode | ObsID       | Date<br>(UT)   | Elapsed Time/<br>Livetime (ks) | Start Epoch<br>(MJD) | Period <sup>a</sup><br>(s) | $Z_1^2$ |
|---------|------------|-------------|----------------|--------------------------------|----------------------|----------------------------|---------|
| XMM     | EPIC-pn/SW | 0606280101  | 2009 Dec 17,18 | 85.1/54.9                      | 55182.820            | 0.112799488(12)            | 173.0   |
| XMM     | EPIC-pn/SW | 0606280201  | 2010 Apr 5     | 42.2/29.4                      | 55291.377            | 0.112799451(20)            | 99.1    |
| XMM     | EPIC-pn/SW | 0650220201  | 2010 May 2     | 28.0/19.6                      | 55318.782            | 0.112799390(41)            | 35.5    |
| Chandra | ACIS-S3/CC | 12108       | 2010 Aug 16    | 34.0/34.0                      | 55424.625            | 0.112799470(21)            | 92.3    |
| XMM     | EPIC-pn/SW | 0650220901  | 2010 Oct 15    | 23.5/16.4                      | 55484.109            | 0.112799519(44)            | 47.0    |
| XMM     | EPIC-pn/SW | 0650221001  | 2010 Oct 15    | 23.5/16.4                      | 55484.987            | 0.112799462(39)            | 56.7    |
| XMM     | EPIC-pn/SW | 0650221101  | 2010 Oct 19    | 26.5/18.6                      | 55488.332            | 0.112799518(40)            | 50.5    |
| XMM     | EPIC-pn/SW | 0650221201  | 2010 Oct 25    | 24.5/17.2                      | 55494.228            | 0.112799486(35)            | 62.1    |
| XMM     | EPIC-pn/SW | 0650221301  | 2010 Nov 12    | 23.5/16.5                      | 55512.524            | 0.112799391(52)            | 44.7    |
| XMM     | EPIC-pn/SW | 0650221401  | 2010 Dec 20    | 27.2/19.0                      | 55550.159            | 0.112799450(35)            | 63.3    |
| Chandra | ACIS-S3/CC | 12109       | 2011 Feb 4     | 33.0/33.0                      | 55596.837            | 0.112799445(27)            | 73.4    |
| XMM     | EPIC-pn/SW | 0650221501  | 2011 Apr 12    | 30.0/21.0                      | 55663.857            | 0.112799449(30)            | 56.6    |
| XMM     | EPIC-pn/SW | 0657600101  | 2011 May 18    | 36.5/25.6                      | 55699.925            | 0.112799480(17)            | 95.6    |
| Chandra | ACIS-S3/CC | 12541       | 2011 Aug 11    | 33.0/33.0                      | 55784.655            | 0.112799412(22)            | 80.4    |
| XMM     | EPIC-pn/SW | 0657600201  | 2011 Nov 8     | 37.2/26.1                      | 55873.289            | 0.112799459(28)            | 42.2    |
| Chandra | ACIS-S3/CC | 12542,14395 | 2012 Feb 18,19 | 33.1/33.1                      | 55975.446            | 0.112799481(35)            | 65.8    |
| XMM     | EPIC-pn/SW | 0657600301  | 2012 Apr 10    | 35.3/24.7                      | 56027.022            | 0.112799445(17)            | 96.5    |

Note. <sup>a</sup> Barycentric period derived from a  $Z_1^2$  test. The Leahy et al. (1983) uncertainty on the last digits is in parentheses.

the time span to 2.3 yr. All of the timing observations used in this analysis are listed in Table 4. The discovery observations from 2001 (Gotthelf & Halpern 2009) are not included, as they are too far removed in time to be reliably connected.

The *Chandra* observations used the Advanced Camera for Imaging and Spectroscopy (ACIS-S3) in CC mode to provide time resolution of 2.85 ms. All data were reprocessed from the level 1 event files with the coordinates corrected for the proper motion of PSR J0821–4300 given in Table 5, and analyzed using the latest calibration files and software (CIAO 4.4/CALDB 4.4.8). Reprocessing with a source position that is accurate to  $<1$  pixel ( $<0\farcs5$ ) ensures that the time assignment is precise to  $\lesssim3$  ms. All of the *XMM-Newton* observations used the pn detector of the European Photon Imaging Camera (EPIC-pn) in “small window” (SW) mode to achieve 5.7 ms time resolution, and an absolute uncertainty of  $\approx3$  ms on the arrival time of any photon. Each data set was examined and cleaned of intervals of high particle background due to solar activity, as necessary. Two pairs of data sets that were acquired on consecutive days were merged to improve their statistics. The photon arrival times from all data were transformed to Barycentric Dynamical Time (TDB) using the coordinates of the pulsar corrected for proper motion.

For PSR J0821–4300, the pulsed signal strength is a strong function of energy, not only because of its spectrum relative to the background but because of the cancellation by emission from the opposite pole, as described in Gotthelf et al. (2010). For each observation listed in Table 4, we extracted source photons using an aperture centered on the source and optimized for the signal strength in the hard 1.5–4.5 keV energy band. For the *XMM-Newton* observations we used an aperture of radius of 30''. For the *Chandra* CC-mode observations we selected five columns (2''.4). We also examined the soft, phase-shifted 0.5–1.0 keV band. However, these data are noisier and their use did not in the end improve the timing results significantly. The phase cancellation effect also prevents pulsations from being detected by the *Chandra* HRC, which has insufficient energy resolution.

As in our previous timing studies of CCOs (Halpern & Gotthelf 2010a, 2011), we employed two complementary ap-

**Table 5**  
Ephemeris of PSR J0821–4300

| Parameter   | Value   |
|---|---|
| Position and proper motion  |   |
| Epoch of position and proper motion (MJD)                         | 53964.0   |
| R.A. (J2000)  | 08 <sup>h</sup> 21 <sup>m</sup> 57 <sup>s</sup> .3653(31) |
| Decl. (J2000)   | -43°00'17.074(43)   |
| R.A. proper motion, $\mu_\alpha \cos \delta$                      | $-54.1 \pm 8.3$ mas yr <sup>-1</sup>                      |
| Decl. proper motion, $\mu_\delta$                                 | $-28.1 \pm 10.5$ mas yr <sup>-1</sup>                     |
| Total proper motion, $\mu$  | $61.0 \pm 8.8$ mas yr <sup>-1</sup>                       |
| Position angle of proper motion                                   | 242°5 ± 9.5   |
| Tangential velocity <sup>a</sup> , $v_{\perp,c}$                  | 629 ± 126 km s <sup>-1</sup>                              |
| Timing solution   |   |
| Epoch of ephemeris (MJD TDB) <sup>b</sup>                         | 55580.0000006   |
| Span of ephemeris (MJD)   | 55,182–56,027   |
| Frequency, $f$  | 8.86529105448(32) Hz                                      |
| Frequency derivative, $\dot{f}$                                   | $(-7.29 \pm 0.28) \times 10^{-16}$ Hz s <sup>-1</sup>     |
| Period, $P$   | 0.1127994550720(41) s                                     |
| Period derivative, $\dot{P}$                                      | $(9.28 \pm 0.36) \times 10^{-18}$                         |
| Kinematic period derivative <sup>a</sup> , $\dot{P}_k$            | $(2.24 \pm 0.72) \times 10^{-18}$                         |
| Intrinsic period derivative <sup>a</sup> , $\dot{P}_{\text{int}}$ | $(7.04 \pm 0.80) \times 10^{-18}$                         |
| Surface dipole magnetic field, $B_s$                              | $2.9 \times 10^{10}$ G                                    |
| Spin-down luminosity, $\dot{E}$                                   | $1.9 \times 10^{32}$ erg s <sup>-1</sup>                  |
| Characteristic age, $\tau_c$                                      | 254 Myr   |

#### Notes.

<sup>a</sup> Assuming  $d = 2.2 \pm 0.3$  kpc (Reynoso et al. 1995).

<sup>b</sup> Epoch of fitted minima of the 1.5–4.5 keV pulse profile; phase zero in Figure 5.

proaches to fitting an ephemeris. First, we used the  $Z_1^2$  (Rayleigh) test (Strutt 1880; Buccheri et al. 1983) in a coherent analysis of the entire set of 17 observations. Beginning with the closely spaced set spanning 2010 October 15–19, the  $Z_1^2$  test determined the pulse frequency with sufficient accuracy to connect in phase uniquely to the next observation. This procedure was iterated by adding each subsequent observation, and including a frequency derivative when it became evident. We also worked backward in time, incorporating all 17 observations in the resulting unique ephemeris. The fitted frequency derivative

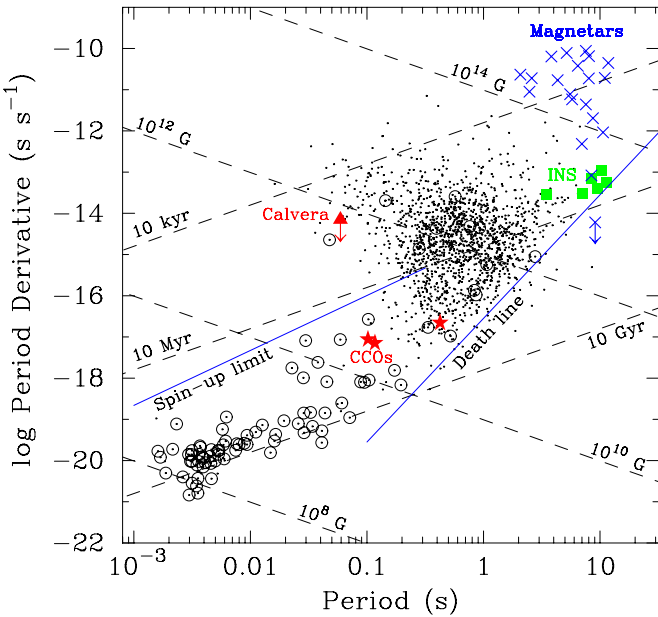


**Figure 3.**  $P-\dot{P}$  diagram of isolated pulsars (dots), binary radio pulsars (circled dots), and other types of isolated X-ray pulsars (colored symbols). The CCO pulsars (red stars) in Kes 79 and Puppis A have virtually the same spin parameters. The upper limit on Calvera’s  $\dot{P}$  is from Halpern (2011). The radio pulsar death line  $B/P^2 = 1.7 \times 10^{11} \text{ G s}^{-2}$  of Bhattacharya et al. (1992) is indicated. The van den Heuvel (1987) spin-up limit for recycled pulsars corresponds to  $P(\text{ms}) = 1.9(B/10^9 \text{ G})^{6/7}$ . The exponent in this equation corrects a typographical error in the caption to Figure 7 of Halpern & Gotthelf (2010a), although the corresponding line in the figure was correct.

(A color version of this figure is available in the online journal.)

is  $\dot{f} = (-6.94 \pm 0.28) \times 10^{-16} \text{ Hz s}^{-1}$ , where the  $1\sigma$  uncertainty comes from the  $\Delta Z_1^2 = -2.3$  contour around the peak power in  $(f, \dot{f})$  space.

The second method also started with the  $Z_1^2$  test statistic, this time to find the period and pulse profile separately at each epoch. The 17 profiles were cross-correlated, shifted, and summed to create a master pulse profile template. The process was iterated to generate a more accurate template and a set of time-of-arrival (TOA) measurements and their uncertainties for each epoch. These TOAs were fitted with a quadratic model in frequency and frequency derivative using a  $\chi^2$  fitting routine to minimize their phase residuals. We searched for a coherent phase-connected solution over a grid of  $f$  and  $\dot{f}$  covering the range  $f = 8.8652906 \pm 0.0000016 \text{ Hz}$  (at epoch MJD 55,580) and  $-3.1 \times 10^{-14} \text{ Hz s}^{-1} < \dot{f} < 1.9 \times 10^{-14} \text{ Hz s}^{-1}$ , with an oversampling factor of 10 for accuracy. This range corresponds to the  $3\sigma$  limits of an incoherent fit to all of the measured frequencies, including the 2001 discovery observations. The resulting frequency derivative from TOA fitting,  $\dot{f} = (-7.29 \pm 0.28) \times 10^{-16} \text{ Hz s}^{-1}$ , is consistent with the value found above from the coherent  $Z_1^2$  search. We adopt the TOA result for the final timing solution listed in Table 5.

The observed  $\dot{P} = (9.28 \pm 0.36) \times 10^{-18}$  can now be split into the sum of its intrinsic and kinematic contributions,  $P = \dot{P}_{\text{int}} + \dot{P}_k$ . Since we determined in Section 2 that  $\dot{P}_k = (2.24 \pm 0.72) \times 10^{-18}$ , the intrinsic period derivative is  $\dot{P}_{\text{int}} = (7.04 \pm 0.80) \times 10^{-18}$ . Parenthetically, we note that the small observed period derivative is independent evidence that the proper motion of the pulsar is not as large as the value originally quoted by Winkler & Petre (2007),  $\mu = 165 \pm 25 \text{ mas yr}^{-1}$ . If so, and if  $d = 2.2 \text{ kpc}$ ,  $\dot{P}_k$  would be  $(1.64 \pm 0.55) \times$

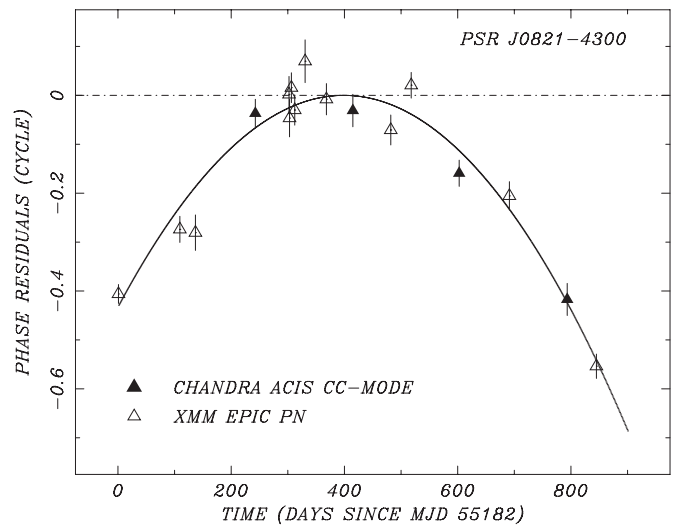


**Figure 4.** For the timing observations of PSR J0821–4300 listed in Table 4, pulse-phase residuals from the linear term (dash-dot line) of the phase ephemeris presented in Table 5. The quadratic term (solid line) contributes  $\approx \pm 0.5$  cycles to the ephemeris over the 2.3 yr of timing.

$10^{-17}$ , requiring  $\dot{P}_{\text{int}}$  to be negative, i.e., the pulsar would be spinning up.

In the vacuum dipole spin-down formalism, the values of  $P$  and  $\dot{P}_{\text{int}}$  imply a surface magnetic field strength  $B_s = 3.2 \times 10^{19} (P \dot{P})^{1/2} \text{ G} = 2.9 \times 10^{10} \text{ G}$ , a spin-down luminosity  $\dot{E} = -I\Omega\dot{\Omega} = 4\pi^2 I \dot{P}/P^3 = 1.9 \times 10^{32} \text{ erg s}^{-1}$ , and characteristic age  $\tau_c \equiv P/2\dot{P} = 254 \text{ Myr}$ . PSR J0821–4300 is nearly identical in its spin properties to PSR J1852+0040 in Kes 79, as shown in Figure 3. The uncertainties in distance and proper motion have only a small effect on the derived magnetic field. For a smaller distance of 1 kpc,  $\dot{P}_k$  is reduced to  $1.02 \times 10^{-17}$ , and  $B_s = 3.1 \times 10^{10} \text{ G}$ . An absolute upper limit regardless of distance and proper motion is  $B_s < 3.3 \times 10^{10} \text{ G}$ .

The phase residuals from the best-fit solution are shown in Figure 4. The weighted rms of the phase residuals is 5.1 ms, or 0.045 pulse cycles, which is comparable to the individual measurement errors (average  $\sigma = 3.6 \text{ ms}$ ). It is not clear whether there is any real timing noise and/or systematic errors in the TOAs.

The light curves of PSR J0821–4300 in the soft and hard bands are shown in Figure 5. These were derived by folding all the timing data on the best-fitting ephemeris given in Table 5. As revealed by a cross-correlation, the soft and hard pulses are out of phase by  $0.45 \pm 0.02$  cycles, consistent with that found by De Luca et al. (2012) using the 2009 December and 2010 April *XMM-Newton* data.

The energy dependence of the pulsar modulation provided an important diagnostic for modeling the viewing geometry and surface emission of PSR J0821–4300 (Gotthelf et al. 2010). By analyzing the light curve in narrower energy bands than in Figure 5, we can resolve the signal modulation and phase for PSR J0821–4300 over the 0.3–5 keV range. The data were grouped into 23 energy bands that are at least 100 eV in width and have a signal-to-noise  $N_s/\sqrt{N_s + N_b} > 100$ , where  $N_s, N_b$  are the source and background counts, respectively. We used  $Z_1^2$  to provide a model of the unbinned light curve. The first Fourier component is a reasonable estimate as the light curve is sinusoidal in each energy band to within counting statistics. The error bar for the phase is calculated by cross-correlation, with the profile of Figure 5 serving as a template.

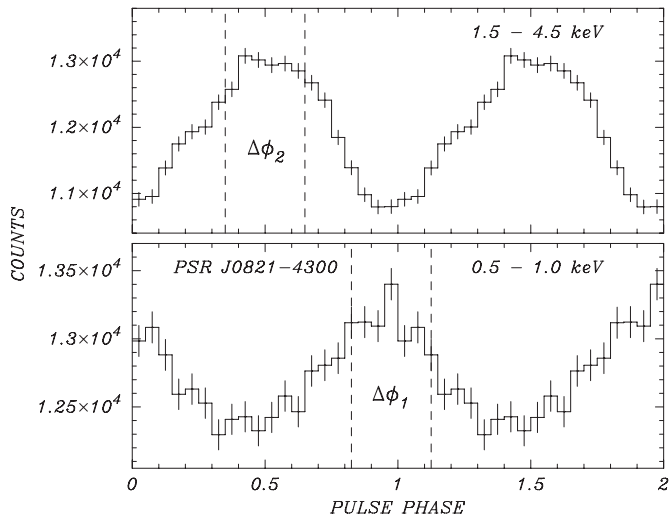


**Figure 5.** Summed pulse profiles of PSR J0821–4300 in the 1.5–4.5 keV band (top) and the 0.5–1.0 keV band (bottom) using all of the observations listed in Table 4, folded according to the ephemeris of Table 5. These hard and soft pulse profiles are out of phase by  $\phi = 0.45 \pm 0.02$  cycles. The intervals between the vertical lines ( $\Delta\phi = 0.3$  cycles) correspond to the two phase regions used in the phase-resolved analysis of Section 4.2 and Table 8.

The result is presented in Figure 6. As the energy dependent modulation decreases, the phase becomes undefined in two energy bands; these two phase points are not plotted. The modulation is qualitatively similar to that predicted by the antipodal model of Gotthelf et al. (2010, cf. their Figure 6), providing confirmation of the basic model. The prediction was based on fitting the modulation in only three energy bands, using much less data, and differs somewhat from the new, resolved data having an order-of-magnitude more counts. In particular, the energy of the minimum modulation is lower (1.12 versus 1.28 keV), and the form of the modulation is more complex than predicted. Furthermore, the phase is seen to drift at lower energies and the transition is not as sharp compared with the antipodal case, in which the phase was statistically either 0.0 or 0.5. The observed characteristics likely imply that the hotspots are offset from a strictly antipodal geometry. The high-quality data presented herein should allow a far more detailed modeling of the surface emission of PSR J0821–4300.

#### 4. SPECTRAL ANALYSIS

Previously, we modeled the original (year 2001) *XMM-Newton* spectra of PSR J0821–4300 as surface blackbody emission from two antipodal spots of different temperatures and areas. Crucially, this model is also able to account for the observed energy-dependent pulse modulation and phase shift (Gotthelf & Halpern 2009; Gotthelf et al. 2010). Additionally, we found evidence of a spectral line feature around 0.8 keV, which more recent data obtained by De Luca et al. (2012) suggest has a time-variable centroid energy. With the increased quantity of data now in hand on PSR J0821–4300, we can re-examine this spectral feature, first by combining all 13 *XMM-Newton* observations presented in Table 4 plus the two observations obtained in 2001, and then by testing for any variability among the observations.

##### 4.1. Summed *XMM-Newton* Spectrum

The spectral analysis presented here uses exclusively the data collected with the EPIC pn. Although background is much

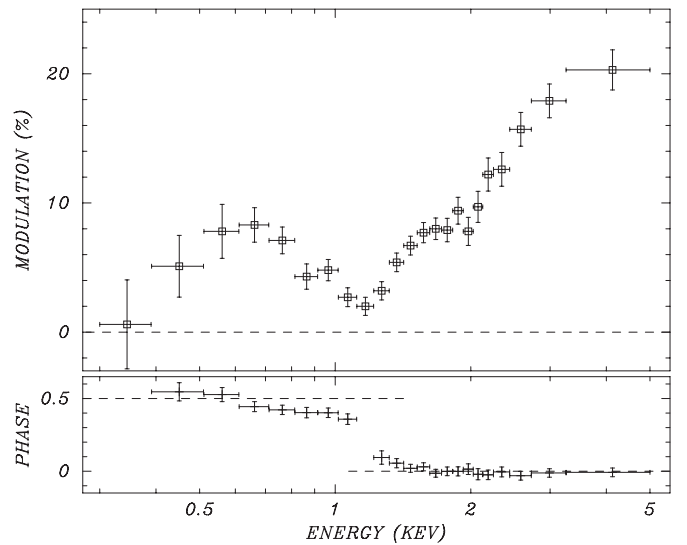


**Figure 6.** Modulation and pulse phase as a function of energy for PSR J0821–4300 using all of the observations listed in Table 4, folded according to the ephemeris of Table 5. The modulation (top) and pulse phase (bottom) reproduce the form predicted for the antipodal model of Gotthelf et al. (2010). Two undefined phase points are omitted.

reduced in the EPIC MOS, this instrument is less sensitive at soft energies, collecting 4.7 times fewer photons than the EPIC pn in the 0.3–1 keV band. Furthermore, much of the EPIC MOS data were lost as the high surface brightness of the Puppis A SNR frequently triggered an automatic shutoff of that detector. We also neglect the *Chandra* ACIS spectra here because of their even poorer low-energy sensitivity and the increased background and other uncertainties involved in the analyzing the *Chandra* CC-mode data. Lastly, one ACIS image taken in timed exposure mode (ObsID 750) suffers from pileup, and was not used.

For the EPIC pn data, the main technical issue is that the SNR background exceeds the point source counts below 1 keV. Surprisingly, the background intensity and spectral shape are both strong functions of spacecraft roll angle. This effect is made evident because the *XMM-Newton* data sets were acquired in two narrow ranges of roll angle roughly 180° apart associated with their respective visibility windows, with the time divided nearly equally between the two. We checked all of our spectral results carefully for features that might be dependent on roll angle due to systematic errors in background subtraction. No such systematic effect were found, which indicates that the background subtraction is reliable in general.

We extracted spectra for each observation from the EPIC pn detector using an aperture of radius 0.3' and a concentric background annulus of  $0.5' < r < 0.6'$ , selecting only events with  $\text{PATTERN} \leq 4$  and  $\text{FLAG} = 0$ . The data were filtered to exclude time intervals of high background identified by count rate  $> 0.1 \text{ s}^{-1}$  in the 10–12 keV energy band. An inspection of the pattern distribution of single and double events shows no evidence of pile-up and suggests that a lower energy bound in the range 0.3–0.4 keV is acceptable. Response matrices and effective area files were generated for each observation using the SAS software suite. We combined data from all observations using the FTOOL *addascaspec* to produce a single source spectrum and associated files. The combined spectrum was grouped to include at least 1000 counts per channel and was fitted using XSPEC v12.21 to a two-blackbody model with

**Table 6**  
Models for the Summed *XMM-Newton* Spectrum of PSR J0821–4300

| Model  | Two Blackbody   | + Emis. Line    | + Abs. Line       | + Two Abs. Lines  | + Cyclabs         |
|--|-----------------|-----------------|-------------------|-------------------|-------------------|
| $N_H$ ( $10^{21}$ cm $^{-2}$ )                             | $3.8 \pm 0.1$   | $4.3 \pm 0.3$   | $3.2 \pm 0.2$     | $2.9 \pm 0.4$     | ...               |
| $kT_w$ (keV)   | $0.26 \pm 0.01$ | $0.25 \pm 0.01$ | $0.29 \pm 0.01$   | $0.29 \pm 0.01$   | $0.28 \pm 0.03$   |
| $kT_h$ (keV)   | $0.46 \pm 0.01$ | $0.45 \pm 0.01$ | $0.49 \pm 0.02$   | $0.49 \pm 0.03$   | $0.47 \pm 0.02$   |
| $L_w(\text{bol})$ ( $10^{33}$ erg s $^{-1}$ ) <sup>a</sup> | $3.3 \pm 0.1$   | $3.6 \pm 0.2$   | $3.1 \pm 0.2$     | $3.0 \pm 0.2$     | $3.2 \pm 0.8$     |
| $L_h(\text{bol})$ ( $10^{33}$ erg s $^{-1}$ ) <sup>a</sup> | $2.0 \pm 0.2$   | $2.0 \pm 0.2$   | $1.4 \pm 0.3$     | $1.4 \pm 0.3$     | $1.7 \pm 0.4$     |
| $A_w$ (km $^2$ )   | $72 \pm 11$     | $89 \pm 18$     | $44 \pm 6$        | $40 \pm 8$        | $53 \pm 14$       |
| $A_h$ (km $^2$ )   | $4.4 \pm 0.9$   | $4.5 \pm 0.9$   | $2.5 \pm 0.8$     | $2.4 \pm 1.0$     | $3.4 \pm 0.8$     |
| $E_0$ (keV)  | ...             | $0.75 \pm 0.01$ | $0.46 \pm 0.05$   | $0.46 \pm 0.01$   | $2E_o$            |
| Width <sup>b</sup> (eV)                                    | ...             | $75 \pm 20$     | $85 \pm 50$       | $106 \pm 20$      | $34\text{--}62$   |
| EW (eV)  | ...             | $53 \pm 10$     | ...               | ...               | $53\text{--}97$   |
| $\tau_o$ <sup>c</sup>                                      | ...             | ...             | $0.1\text{--}0.9$ | $0.6\text{--}1.3$ | $0.9\text{--}1.7$ |
| $\chi^2$ (dof)   | 1.50(359)       | 1.08(356)       | 1.16(356)         | 1.08(354)         | 1.12(354)         |

**Notes.** The  $1\sigma$  uncertainties for three interesting parameters ( $\Delta\chi^2 = 3.53$ ) are given.

<sup>a</sup> Blackbody bolometric luminosity for a distance of 2.2 kpc.

<sup>b</sup> Gaussian  $\sigma$  for the emission or absorption lines, natural width  $W$  for the cyclotron absorption model (Makishima et al. 1990; Mihara et al. 1990).

<sup>c</sup> Optical depth at line center.

interstellar absorption over the energy range 0.3–5 keV (see Figure 7 and Table 6).

The resulting high signal-to-noise ratio of the fitted spectrum reveals significant features that are unaccounted for by the two-blackbody model. The best-fit model, with  $N_H = (3.8 \pm 0.01) \times 10^{21}$  cm $^{-2}$ ,  $kT_w = 0.26 \pm 0.01$  keV, and  $kT_h = 0.46 \pm 0.01$  keV, has reduced  $\chi^2_v = 1.50$  for 359 degrees of freedom (dof), which is formally unacceptable. The deviations are evident in structure in the residuals in Figure 7(a). Adding a Gaussian emission line to the model as suggested by our previous work improves the fit to  $\chi^2_v = 1.08$  for 358 dof (Figure 7(b)). The centroid energy of the line is  $0.75 \pm 0.01$  keV, and its equivalent width is  $53 \pm 10$  eV.

Considering the shape of the residuals from the two-blackbody fit in Figure 7(a), an alternative hypothesis is that an absorption feature, or features, is responsible. Accordingly we applied a Gaussian absorption line, two Gaussian absorption lines, and finally, the cyclotron absorption model of Makishima et al. (1990) and Mihara et al. (1990), which is available in XSPEC as cyclabs. As shown in Table 6 and Figure 8, all of these models gave acceptable fits. Two absorption lines, when fitted independently, are separated by nearly a factor of two in energy, which is suggestive of the fundamental and first harmonic in a cyclotron model. Therefore, we fixed the ratio of their centroid energies at 2, with the result that their centroids are at 0.46 keV and 0.92 keV, bracketing the energy previously ascribed to an emission line. The cyclabs model, which also fixes this ratio, yields the same centroid energies. We conclude that, from the phase-averaged spectra alone, it is not possible to distinguish an emission feature from one or two absorption lines, which leaves the physical interpretation uncertain.

The fundamental energy of the electron cyclotron resonance falls at

$$E_0 = 1.16(B/10^{11}\text{ G})/(1+z)\text{ keV}, \quad (2)$$

where  $z$  is the gravitational redshift. Assuming a typical value of  $z = 0.3$ , and if  $B \approx B_s = 2.9 \times 10^{10}$  G, the equatorial field from the vacuum dipole spin-down result, then  $E_0 \approx 0.26$  keV is expected. When compared with  $E_0 = 0.46$  keV from the absorption-line fit, or 0.75 keV from the emission-line fit, this hints that the local surface field where the line is formed is larger than the equatorial dipole field, but is perhaps more compatible with the field at the pole,  $B_p = 2B_s$ . Other factors possibly affecting a comparison between the dipole spin-down

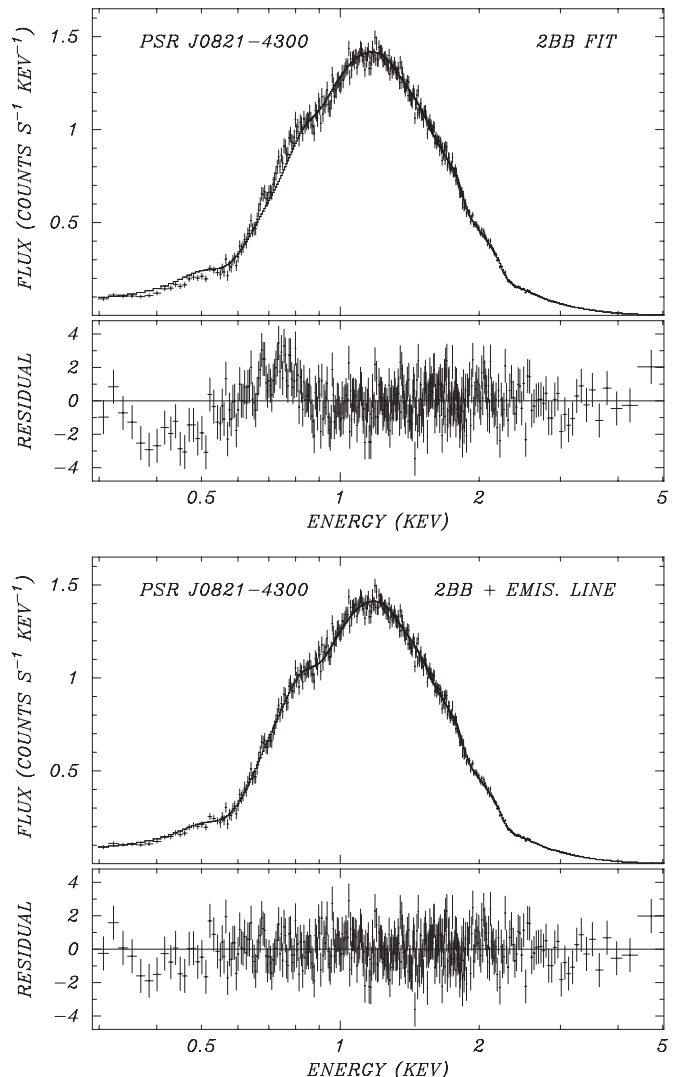


**Figure 7.** (a) EPIC pn spectrum of the 16 summed *XMM-Newton* observations of PSR J0821–4300 fitted to a double-blackbody model. The residuals from the fit are shown in the bottom panel. (b) The same spectrum fitted with a double-blackbody model plus Gaussian emission line. The parameters of these fits are given in Table 6.

**Table 7**  
Individual *XMM-Newton* Spectra of PSR J0821–4300

| Group | ObsID       | Livetime<br>(ks) | $kT_w$<br>(keV)  | $kT_h$<br>(keV)  | Flux<br>( $10^{-12}$ erg s $^{-1}$ cm $^{-2}$ ) | $\chi^2_{\nu}$ (dof) |
|-------|-------------|------------------|------------------|------------------|---|----------------------|
| 1     | 0113020101S | 15.2             | 0.27(0.25, 0.29) | 0.47(0.44, 0.52) | 4.23(4.14, 4.30)                                | 1.06(154)            |
|       | 0113020301S | 16.1             | 0.27(0.25, 0.28) | 0.46(0.43, 0.50) | 4.21(4.12, 4.27)                                | 1.05(184)            |
| 2     | 0606280101S | 25.7             | 0.27(0.26, 0.28) | 0.47(0.45, 0.51) | 4.15(4.09, 4.20)                                | 1.19(282)            |
|       | 0606280101U | 24.5             | 0.25(0.24, 0.26) | 0.45(0.43, 0.47) | 4.11(4.05, 4.16)                                | 0.91(268)            |
|       | 0606280201S | 24.6             | 0.27(0.26, 0.28) | 0.47(0.45, 0.50) | 4.14(4.09, 4.20)                                | 1.02(261)            |
|       | 0650220201S | 8.1              | 0.22(0.19, 0.26) | 0.40(0.38, 0.45) | 4.11(4.01, 4.20)                                | 0.88(94)             |
| 3     | 0650220901S | 16.4             | 0.25(0.24, 0.27) | 0.45(0.42, 0.48) | 4.13(4.06, 4.19)                                | 1.01(191)            |
|       | 0650221001S | 15.5             | 0.24(0.22, 0.25) | 0.42(0.40, 0.44) | 4.13(4.06, 4.20)                                | 0.99(183)            |
|       | 0650221101S | 18.6             | 0.26(0.25, 0.28) | 0.48(0.45, 0.51) | 4.19(4.12, 4.25)                                | 0.97(222)            |
|       | 0650221201S | 17.1             | 0.27(0.26, 0.28) | 0.49(0.46, 0.54) | 4.17(4.08, 4.23)                                | 1.08(201)            |
|       | 0650221301S | 16.4             | 0.28(0.27, 0.29) | 0.52(0.48, 0.57) | 4.06(3.98, 4.12)                                | 1.21(182)            |
|       | 0650221401S | 15.5             | 0.24(0.23, 0.26) | 0.43(0.41, 0.46) | 4.13(4.05, 4.20)                                | 1.00(174)            |
| 4     | 0650221501S | 20.3             | 0.27(0.25, 0.28) | 0.45(0.43, 0.48) | 4.26(4.20, 4.32)                                | 0.96(225)            |
|       | 0657600101S | 22.4             | 0.26(0.25, 0.27) | 0.47(0.44, 0.50) | 4.13(4.07, 4.19)                                | 0.99(242)            |
|       | 0657600201S | 26.1             | 0.26(0.25, 0.27) | 0.45(0.43, 0.47) | 4.24(4.19, 4.30)                                | 1.07(285)            |
|       | 0657600301S | 24.7             | 0.26(0.25, 0.28) | 0.46(0.44, 0.49) | 4.22(4.16, 4.27)                                | 0.94(262)            |

**Notes.** Results for a fit to an absorbed, two-blackbody model with the column density held fixed at  $N_H = 3.75 \times 10^{21}$  cm $^{-2}$ , the value obtained for the summed spectrum in Table 6. The absorbed flux in the 0.5–5 keV range is tabulated. The range of uncertainty of each value is the  $1\sigma$  confidence interval for two interesting parameters.

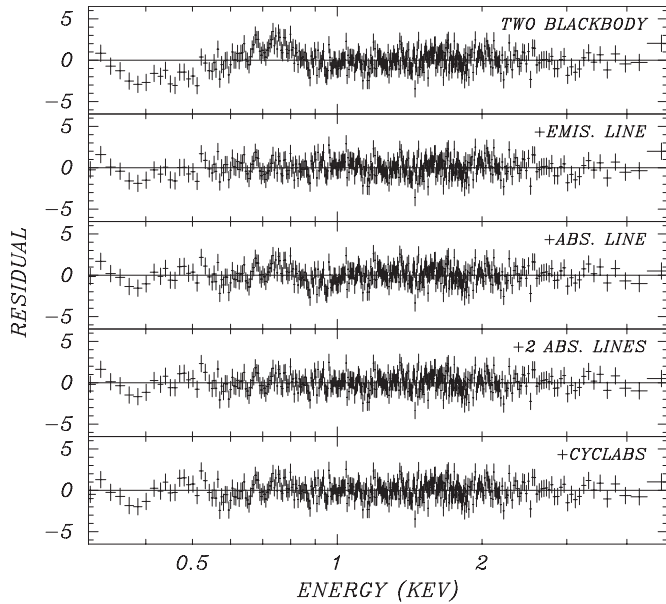


**Figure 8.** Same as Figure 7 but showing the residuals from fits to a double-blackbody model plus, from top to bottom: no line, a Gaussian emission line, a Gaussian absorption line, two Gaussian absorption lines, and a cyclotron absorption line model. The parameters of the fits are given in Table 6.

*B*-field and the surface *B*-field from the cyclotron energy will be explored in Section 6.2.

The addition of emission or absorption lines to the model near the low-energy end of the *XMM-Newton* spectrum affects the fitted value of the column density  $N_H$ , with values ranging from  $(2.8\text{--}4.3) \times 10^{21}$  cm $^{-2}$  for the different models in Table 6. Therefore, it is possible that comparison with independent measurements of  $N_H$  may suggest a preference for one or another of these models. For example, the 21 cm H I emission in the foreground of Puppis A amounts to  $N_{\text{H}_1} = 2.5 \times 10^{21}$  cm $^{-2}$  according to Reynoso et al. (2003). To obtain this value, they integrated the H I line emission in the radial velocity range  $-10$

to  $+16$  km s $^{-1}$ , the latter velocity corresponding to their assumed 2.2 kpc distance of Puppis A. Comparison with the values of  $N_H$  in Table 6 tends to favor the X-ray spectral models that include absorption lines. While this agreement is encouraging, it is subject to the caveat that the 21 cm column density is formally a lower limit, assuming as it does that the line is optically thin. Better support for a low column density comes from the *XMM-Newton* RGS spectra of several regions of the Puppis A SNR fitted by Katsuda et al. (2012). These require X-ray  $N_H$  in the range  $(2.58\text{--}2.85) \times 10^{21}$  cm $^{-2}$ , which also agrees closely with the  $N_H$  from our absorption-line models for the pulsar spectrum.

Finally, we note that the total luminosity and blackbody areas reported in Table 6 differ from those presented in Gotthelf & Halpern (2009), the areas by a factor of two or more. This is a consequence of the best-fit values for each model fit. The derived blackbody areas depend on blackbody temperature as  $T^{-4}$ , which itself is strongly correlated with the fitted column density. Future work, simultaneously modeling of the phase-dependent spectra, should better constrain the column density and temperatures, and consequently provide a more accurate measurement of the blackbody areas.

#### 4.2. Search for Variability

To test for long-term variability of PSR J0821–4300, we also fitted the individual *XMM-Newton* spectra, searching for temperature variations on the surface, for example. The spectra for each observation are well fitted by the two-blackbody model, with parameters listed in Table 7; their statistics do not warrant an additional line component. For this comparison, we held the absorbing column fixed at the value in Table 6 derived from the fit of the composite spectrum to the two-blackbody model. Figure 9 displays the results. No significant variation is evident in the flux or in either of the two blackbody temperatures.

We next test for pulse-phase dependence of the spectral line feature(s) by generating spectra in two phase intervals, each of  $\Delta\phi = 0.3$  cycles in width centered on the peaks of the soft and hard light curves, respectively (see Figure 5.). This is

**Table 8**  
*XMM-Newton* Phase-resolved Spectra of PSR J0821–4300

| Model Parameter         | Group 1<br>2001 Apr–Nov | Group 2<br>2009 Dec to 2010 May | Group 3<br>2010 Oct–Dec | Group 4<br>2011 Apr to 2012 Apr | Sum<br>2001 Apr to 2012 Apr |
|-------------------------|-------------------------|---------------------------------|-------------------------|---------------------------------|-----------------------------|
| $kT_w$ (keV)            | 0.23(0.21, 0.25)        | 0.25(0.24, 0.26)                | 0.24(0.23, 0.25)        | 0.27(0.25, 0.28)                | 0.25(0.24, 0.25)            |
| $kT_h$ (keV)            | 0.41(0.39, 0.44)        | 0.45(0.43, 0.47)                | 0.44(0.42, 0.46)        | 0.47(0.44, 0.52)                | 0.44(0.43, 0.45)            |
| $F[\Delta\phi_1]^a$     | 4.00(3.97, 4.08)        | 3.91(3.88, 3.93)                | 3.94(3.91, 3.96)        | 3.99(3.96, 4.01)                | 3.96(3.94, 3.97)            |
| $F[\Delta\phi_2]^a$     | 4.33(4.28, 4.38)        | 4.37(4.35, 4.40)                | 4.37(4.34, 4.39)        | 4.45(4.42, 4.47)                | 4.40(4.38, 4.41)            |
| $E_0$ (keV)             | 0.79(0.76, 0.81)        | 0.71(0.68, 0.73)                | 0.72(0.69, 0.74)        | 0.69(0.63, 0.73)                | 0.72(0.70, 0.73)            |
| $\sigma$ (eV)           | $\leq 62$               | 44(21, 70)                      | 68(45, 95)              | 133(78, 195)                    | 69(52, 89)                  |
| $EW[\Delta\phi_1]$ (eV) | 40(24, 51)              | 77(59, 89)                      | 58(46, 76)              | 86(67, 107)                     | 61(53, 74)                  |
| $EW[\Delta\phi_2]$ (eV) | 14(3, 22)               | 34(23, 42)                      | 42(32, 57)              | 39(26, 52)                      | 31(26, 39)                  |
| $\chi^2_v$ (dof)        | 1.01(87)                | 1.19(229)                       | 1.05(269)               | 0.99(250)                       | 1.20(212)                   |

**Notes.** Results from simultaneous fits to *XMM-Newton* spectra of PSR J0821–4300 extracted from two pulse-phase intervals,  $\Delta\phi_1$ ,  $\Delta\phi_2$ , as defined in the Figure 5. Group numbers are defined in Table 7. The blackbody temperatures and Gaussian line energy are linked between the two phases. The column density is fixed at  $N_H = 4.28 \times 10^{21} \text{ cm}^{-2}$ , the phase-averaged value for the summed spectrum in Table 6. Quoted uncertainties are  $1\sigma$  for three interesting parameters.

<sup>a</sup> Absorbed flux quoted for the 0.5–5.0 keV band in units of  $10^{-12} \text{ erg s}^{-1} \text{ cm}^{-2}$ .

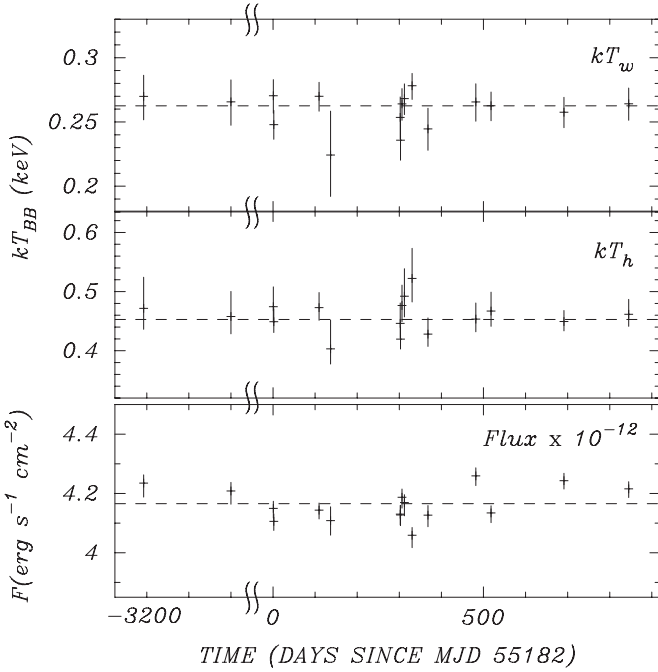


**Figure 9.** Blackbody temperatures and flux in the 0.5–5 keV band for the 16 individual *XMM-Newton* observations of PSR J0821–4300, fitted to the two-blackbody model. Data are taken from Table 7. Errors bars are  $1\sigma$ . The weighted mean values are indicated by the dashed lines.

motivated by the original finding in Gotthelf & Halpern (2009) that an emission line is more strongly associated with the warm region, i.e., the soft phase of the pulse. For simplicity, given the reduced counts in the phased spectra, we used only the Gaussian emission-line model as a representative for all of the possible line models. The two phase-resolved spectra combined from all epochs are shown in Figure 10, where they are fitted to the two-blackbody plus Gaussian emission-line model. In the simultaneous fit, the two temperatures and the line centroid energy are linked. As shown in Table 8, the equivalent width of the Gaussian line is indeed about factor of two larger in the soft-phase spectrum than in the hard-phase.

De Luca et al. (2012) presented evidence that the emission-line centroid had decreased from 0.80 keV to 0.73 keV between 2001 and 2009. Here we extend the examination for variability of the spectral feature, including its phase dependence, by

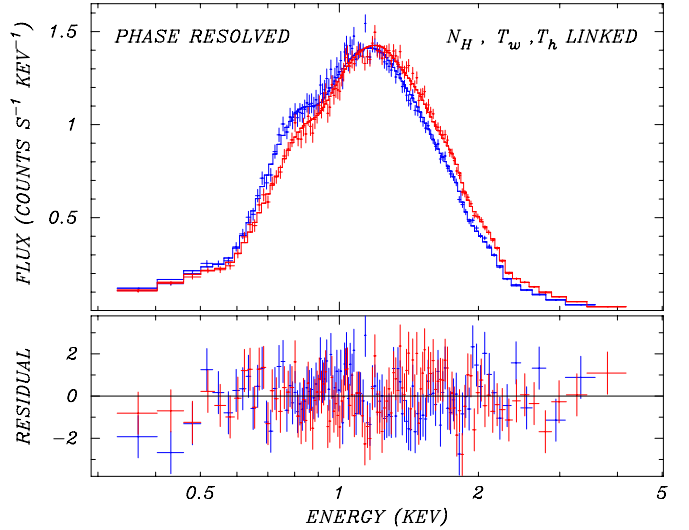


**Figure 10.** Combined *XMM-Newton* EPIC pn spectrum of PSR J0821–4300 in two pulse-phase intervals defined in Figure 5 ( $\Delta\phi_1$ , blue,  $\Delta\phi_2$ , red), fitted to a double-blackbody model plus Gaussian emission line. The blackbody temperatures and line centroid energy are linked between the two spectra. The fitted parameters are given in the last column of Table 8. The residuals to the fit are shown in the bottom panel.

(A color version of this figure is available in the online journal.)

combining the *XMM-Newton* spectra into four groups of adjacent observations as indicated Table 7. We fitted these four sets of spectra to the two blackbody plus Gaussian emission-line model, with their temperatures and line width (sigma) linked between the two phase intervals. The four fits are displayed in Figure 11, and the fitted parameters for each set and their sum are presented in Table 8. It is clear that the temperatures and their contributed fluxes are steady in time, consistent with their phase-averaged behavior and with no time dependence in their phase ratios. On the other hand, the equivalent width of the fitted Gaussian emission line shows evidence for having increased between 2001 and 2009, while the line centroid energy decreased from  $0.79^{+0.02}_{-0.03}$  keV to  $0.71^{+0.02}_{-0.03}$  keV. While these results are consistent with the De Luca et al. (2012) analysis of the same data, there is little if any additional variability between 2009 and 2012.

We also repeated this test for variability with the Gaussian absorption-line model for the spectral feature (results not tabulated here). For either the emission-line or the

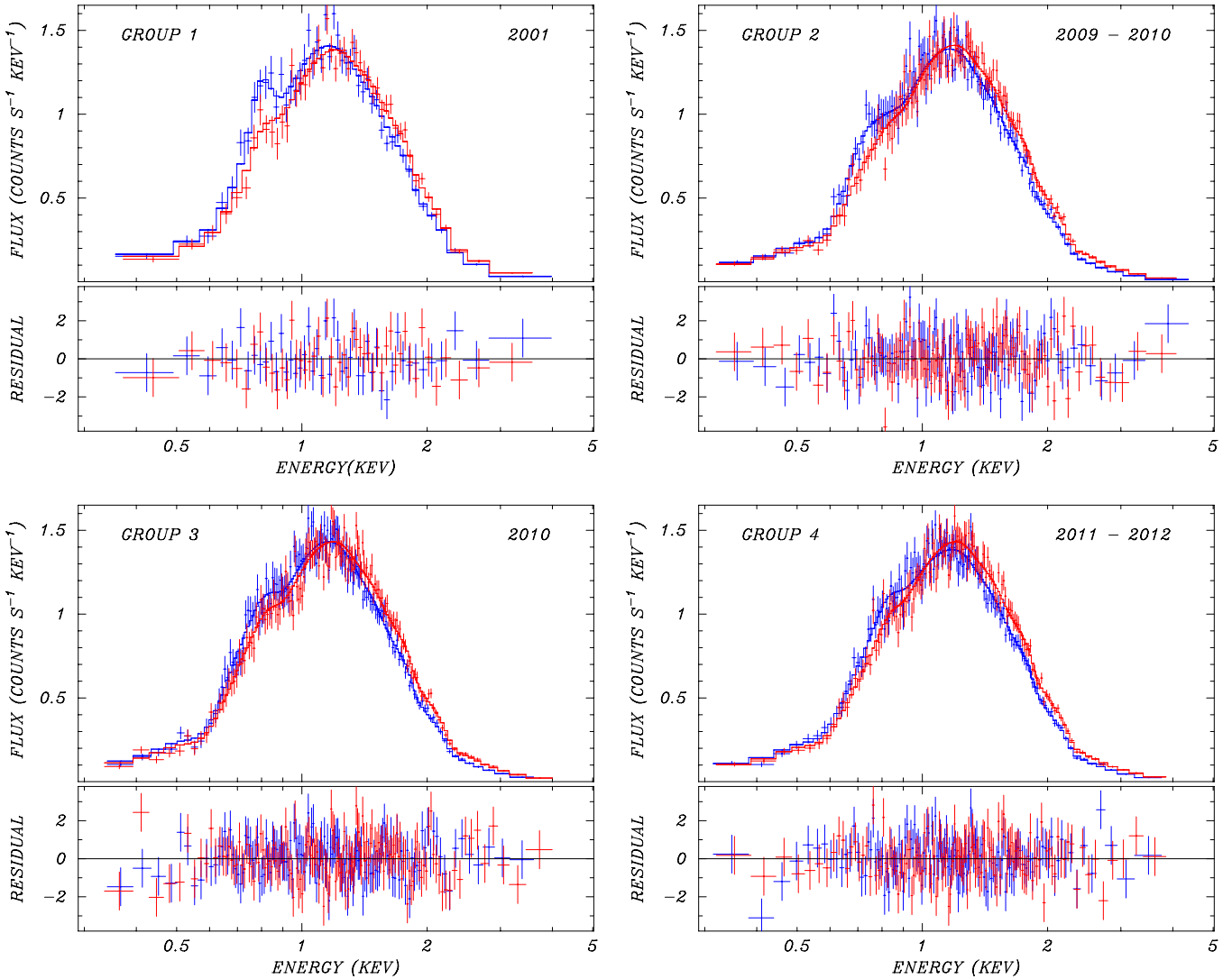


**Figure 11.** *XMM-Newton* EPIC pn spectra of PSR J0821–4300, grouped into the four sets as listed in Table 7, and fitted to a double-blackbody model with Gaussian emission line. As in Figure 10, red and blue represent the two pulse-phase intervals defined in Figure 5. The residuals from the fits are shown in the bottom panels. The fitted parameters are given in Table 8.

(A color version of this figure is available in the online journal.)

absorption-line model, the measured line centroids for all epochs but 2001 cluster well within their  $1\sigma$  uncertainty (for two interesting parameters,  $\Delta\chi^2 = 2.3$ ). The 2001 set deviates from the mean defined by the other three sets by  $\approx 2\sigma$ . In terms of percentage deviation from the mean, the line centroid measured in 2001 was 14% and 8% higher in the emission line and the absorption line model, respectively. We conclude that, although the deviation seems large for the emission line model, it is not inconsistent with the expected variance. Further observations would be necessary to establish more definite evidence of long-term variability.

## 5. A DEFINITIVE SPIN-DOWN MEASUREMENT FOR PSR J1210–5226

Archival timing observations of PSR J1210–5226 spanning the years 2000–2008 were too sparse to securely determine its spin-down rate, as described in Halpern & Gotthelf (2011). Searching all possible parameter space for a phase-coherent, quadratic ephemeris, we found two equally acceptable solutions, with  $f = -1.243(22) \times 10^{-16}$  Hz s<sup>-1</sup> and  $f = -7.084(22) \times$

$10^{-16}$  Hz s<sup>-1</sup>, corresponding to  $B_s = 9.9 \times 10^{10}$  G (solution 1) and  $B_s = 2.4 \times 10^{11}$  G (solution 2), respectively. Since such low  $\dot{E}$  pulsars are generally very stable rotators with little timing noise or glitch activity, it was deemed likely that one of these is the true solution, and the other one is an alias with an incorrect cycle count. It is also important that no solutions with smaller dipole  $B_s$ , and no spinning-up solutions, were found.

In 2011–2012 we started a new series of observations of PSR J1210–5226 with *Chandra* and *XMM-Newton* that was designed to initiate and maintain a unique, phase-connect timing solution of this pulsar for the first time and eliminate the prior timing ambiguity. Table 9 is a log of the new observations. The instrumental setups and analysis methods are the same as those described in Section 3 for PSR J0821–4300, except that the *XMM-Newton* source photons were extracted from a 20'' radius aperture instead of 30'', and the 0.5–2.5 keV band was selected to optimize the pulsed signal.

The coherently measured period from the new observations is precise enough to reject previous timing solution 2, while solution 1 with the smaller  $B_s$  extrapolates precisely to the new period. Furthermore, the new pulse phases are aligned accurately

**Table 9**  
Log of New X-Ray Timing Observations of PSR J1210–5226

| Mission        | Instr/Mode | ObsID      | Date<br>(UT) | Exposure<br>(ks) | Start Epoch<br>(MJD) | Frequency <sup>a</sup><br>(Hz) | $Z_1^2$ |
|----------------|------------|------------|--------------|------------------|----------------------|--------------------------------|---------|
| <i>Chandra</i> | ACIS-S3/CC | 14199      | 2011 Nov 25  | 31.0             | 55890.233            | 2.3577625(28)                  | 48.2    |
| <i>Chandra</i> | ACIS-S3/CC | 14202      | 2012 Apr 10  | 33.0             | 56027.637            | 2.3577709(43)                  | 22.2    |
| <i>XMM</i>     | EPIC-pn/SW | 0679590101 | 2012 Jun 22  | 26.5             | 56100.537            | 2.3577687(25)                  | 68.3    |
| <i>XMM</i>     | EPIC-pn/SW | 0679590201 | 2012 Jun 24  | 22.3             | 56102.752            | 2.3577621(34)                  | 69.0    |
| <i>XMM</i>     | EPIC-pn/SW | 0679590301 | 2012 Jun 28  | 24.9             | 56106.490            | 2.3577636(23)                  | 109.6   |
| <i>XMM</i>     | EPIC-pn/SW | 0679590401 | 2012 Jul 2   | 24.5             | 56110.918            | 2.3577626(28)                  | 61.4    |
| <i>XMM</i>     | EPIC-pn/SW | 0679590501 | 2012 Jul 18  | 27.3             | 56126.553            | 2.3577640(27)                  | 51.9    |
| <i>XMM</i>     | EPIC-pn/SW | 0679590601 | 2012 Aug 11  | 27.3             | 56150.408            | 2.3577637(23)                  | 81.8    |
| <i>Chandra</i> | ACIS-S3/CC | 14200      | 2012 Dec 1   | 31.1             | 56262.095            | 2.3577634(28)                  | 39.8    |

**Note.** <sup>a</sup> Barycentric frequency derived from a  $Z_1^2$  test. The given uncertainty is for the  $1\sigma$  confidence interval.

**Table 10**  
Ephemeris of PSR J1210–5226

| Parameter                                 | Value   |
|---|---|
| R.A. (J2000) <sup>a</sup>                 | 12 <sup>h</sup> 10 <sup>m</sup> 00 <sup>s</sup> .91       |
| Decl. (J2000) <sup>a</sup>                | -52°26'28".4  |
| Epoch of ephemeris (MJD TDB) <sup>b</sup> | 53562.0000006   |
| Span of ephemeris (MJD)                   | 51,549–56,262   |
| Frequency, $f$                            | 2.357763502865(65) Hz                                     |
| Frequency derivative, $\dot{f}$           | $(-1.2363 \pm 0.0091) \times 10^{-16}$ Hz s <sup>-1</sup> |
| Period, $P$                               | 0.424130748816(12) s                                      |
| Period derivative, $\dot{P}$              | $(2.224 \pm 0.016) \times 10^{-17}$                       |
| Surface dipole magnetic field, $B_s$      | $9.8 \times 10^{10}$ G                                    |
| Spin-down luminosity, $\dot{E}$           | $1.2 \times 10^{31}$ erg s <sup>-1</sup>                  |
| Characteristic age, $\tau_c$              | 302 Myr   |

#### Notes.

<sup>a</sup> Measured from *Chandra* ACIS-S3 ObsID 3913. Typical uncertainty is 0''.6.

<sup>b</sup> Epoch of fitted minima of summed pulse profile; phase zero in Figure 13

with solution 1, while solution 2 gives random phases. Thus a unique quadratic ephemeris fits all 12.9 yr of *Chandra* and *XMM-Newton* timing. Table 10 gives this global ephemeris, derived from a least-squares fit to the TOAs as described in Section 3, with the phase residuals shown in Figure 12. The previous uncertainty on the  $\dot{f}$  of solution 1 is reduced by a factor of two, with the result  $\dot{f} = -1.2363(91) \times 10^{-16}$  Hz s<sup>-1</sup>; the corresponding dipole magnetic field is  $B_s = 9.8 \times 10^{10}$  G. Figure 13 shows the pulse profile using data from all the observations folded on the presented ephemeris.

Strictly speaking, the derived period derivative is an upper limit to the intrinsic one, as any proper motion has not been measured and taken into account. PSR J1210–5226 and PSR J0821–4300 are at similar distances, and the location of PSR J1210–5226 with respect to the geometric center of SNR PKS 1209–51/52 allows (but does not require, since the kinematics of the SNR are unknown) a proper motion of  $\sim 70$  mas yr<sup>-1</sup>, or  $v_{\perp} \sim 730$  km s<sup>-1</sup> (De Luca et al. 2011), similar to that of PSR J0821–4300. If so, the Shklovskii effect given by Equation (1) would contribute  $\dot{P}_k \sim 1.1 \times 10^{-17}$ , or half of the total  $\dot{P}$ , and the spin-down dipole field would be reduced somewhat, to  $B_s \approx 7 \times 10^{10}$  G. Of course, if these two CCOs both have velocities toward the high end of the distribution of pulsars, it would be a tantalizing physical result in itself. However, examination of another CCO, the NS in Cas A, does not necessarily support such high velocities for CCOs, in general; Thorstensen et al. (2001) and Fesen et al. (2006) find  $v_{\perp} \approx 350$  km s<sup>-1</sup> with respect to the explosion center of Cas A.

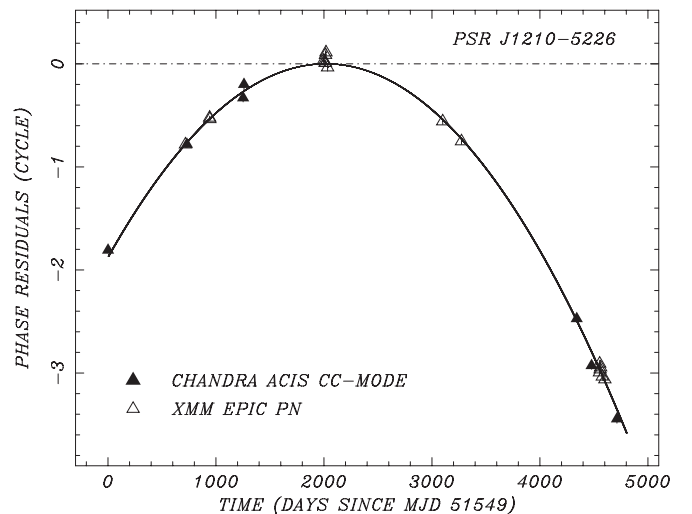


**Figure 12.** Pulse-phase residuals from the linear term (dash-dot line) of the phase ephemeris of PSR J1210–5226 presented in Table 10. Included are the new observations listed in Table 9 and the archival timing observations from Table 1 of Halpern & Gotthelf (2011). The quadratic term (solid line) corresponds to the uniquely determined period derivative spanning the years 2000–2012. The error bars are generally smaller than the symbol size.

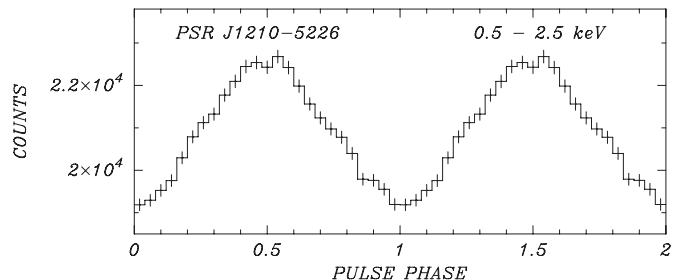


**Figure 13.** Pulse profiles of PSR J1210–5226 in the 0.5–2.5 keV band using data from all timing observations, folded according to the ephemeris in Table 10. Phase zero corresponds to the listed TDB epoch of the ephemeris. Included are the new observations in Table 9 and the archival timing observations from Table 1 of Halpern & Gotthelf (2011).

## 6. DISCUSSION

### 6.1. On the Age of Puppis A

Becker et al. (2012) discussed the impact of the revised proper motion of PSR J0821–4300 on the inferred age of Puppis A. The age of the SNR had been derived previously as  $3700 \pm 300$  yr from the proper motions of optical filaments

that point back to a common center, presumed to be the site of the explosion, and assuming no deceleration. The motion of the NS also extrapolates to the same center, but the distance traveled,  $371'' \pm 31''$ , corresponds to an age of  $5200 \pm 1000$  yr (or  $6100 \pm 1000$  yr for our proper motion of  $61 \pm 9$  mas yr $^{-1}$ ). Becker et al. (2012) refer to these marginally contradictory measurements as independent, and choose to average them, giving the value 4.5 kyr listed in Table 1. However, they are not truly independent because they assume the same starting location. Furthermore, the discrepancy is worse if the filaments have decelerated. Just as the new *Chandra* observations of the NS have improved the accuracy of its proper motion, we suggest that a contemporary observation of the optical filaments of Puppis A may improve the precision of the original Winkler et al. (1988) study on which the optical proper-motion age is based. Such an investigation could lead to a more detailed understanding of dynamics of the filaments, and a more accurate age for Puppis A.

### 6.2. PSR J0821–4300 and PSR J1210–5226 as Anti-magnetars

The spin-down of power PSR J0821–4300,  $\dot{E} = 1.9 \times 10^{32}$  erg s $^{-1}$ , is consistent with being caused by magnetic braking of an isolated neutron star (INS) with a weak dipole field of  $B_s = 2.9 \times 10^{10}$  G. Its spin-down power is much smaller than its observed thermal X-ray luminosity,  $L_x \approx 5.6 \times 10^{33} d_{2.2}^2$  erg s $^{-1}$ , which rules out rotation as a significant power source. As discussed in Halpern & Gotthelf (2010a) for PSR J1852+0040, the very small  $\dot{P}$  disfavors propeller spin-down and accretion as a source of the X-rays. Thus, residual cooling remains the most plausible source of the X-ray luminosity of PSR J0821–4300 and, by extension, of all CCOs. Given the meager spin-down power of PSR J0821–4300, we can also discount the suggestion of Reynoso et al. (2003) and Castelletti et al. (2006) that structure in the Puppis A SNR and associated H I is caused by jets emitted by the pulsar, similar to the SS433/W50 system. Parenthetically, if the H I morphology is not caused by the pulsar, then it does not provide supporting evidence of its distance.

An unresolved question about PSR J0821–4300 is the origin of its phase-dependent, possibly variable emission or absorption feature. In the absence of accretion, it would be difficult to understand how an emission line is generated, or why it would vary in a few years. The indication of variability is not strong, and there is no other evidence of accretion. Therefore, we will consider here an absorption-line interpretation, for which there is a good precedent in PSR J1210–5226, the only isolated pulsar to show a series of strong absorption lines in its spectrum (Sanwal et al. 2002; Mereghetti et al. 2002a; Bignami et al. 2003).

The spectral features in PSR J1210–5226 are now widely considered to comprise the electron cyclotron fundamental at  $E_0 = 0.7$  keV and its harmonics. The surface magnetic field strength where the lines are formed is inferred to be  $B \approx 8 \times 10^{10}$  G according to Equation (2) and assuming  $z \approx 0.3$ . The relative strength of the harmonics is explained by treating them as resonances in the photospheric free-free opacity in the presence of the magnetic field (Suleimanov et al. 2010, 2012). PSR J1210–5226 is exceptional in having the largest known spin-down dipole magnetic field among CCOs, now confirmed as  $B_s \leq 9.8 \times 10^{10}$  G. This is only slightly larger than  $B \approx 8 \times 10^{10}$  G inferred from the spectral features, and is the first case in which such a comparison has been made

between independent methods of measuring surface  $B$ -field on an isolated pulsar. Effects that could eliminate the already minor discrepancy include the unmeasured proper motion, which would decrease the inferred spin-down dipole field, and the results of numerical models of a force-free magnetosphere, which imply a different spin-down law from the standard vacuum dipole expression

$$B_s = \left( \frac{3c^3 I P \dot{P}}{8\pi^2 R^6 \sin^2 \alpha} \right)^{1/2} = 3.2 \times 10^{19} \left( \frac{P \dot{P}}{\sin^2 \alpha} \right)^{1/2} \text{ G} \quad (3)$$

such that, more accurately,

$$B_s \approx \left( \frac{c^3 I P \dot{P}}{4\pi^2 R^6 [1 + \sin^2 \alpha]} \right)^{1/2} = 2.6 \times 10^{19} \left( \frac{P \dot{P}}{1 + \sin^2 \alpha} \right)^{1/2} \text{ G} \quad (4)$$

(Spitkovsky 2006). This means that a measured spin-down rate is obtained with  $B_s$  smaller by a factor 0.58–0.82 than the conventional approximation  $B_s = 3.2 \times 10^{19} (P \dot{P})^{1/2}$  G.

In the case of PSR J0821–4300, by the same logic, its weaker inferred dipole magnetic field of  $B_s \leq 2.9 \times 10^{10}$  G would not naturally account for a spectral feature at 0.7–0.8 keV, instead predicting  $E_0 \leq 0.26$  keV. The absorption model with the cyclotron fundamental at  $E_0 = 0.46$  keV comes closer to the prediction. However, additional variables can affect the comparison of a dipole field inferred from spin-down with that from a cyclotron line. First is the factor of two variation of dipole field strength over the surface, with  $B_p = 2 B_s$ . Second, the actual field is not likely to be a centered dipole, and may be larger than  $B_s$  or  $B_p$  in places where the line is formed. The asymmetric distribution of surface temperature on PSR J0821–4300 already appears to require a complex magnetic field geometry, such as an off-center dipole or higher multipoles. Third, the inferred spin-down field depends on the uncertain NS mass and radius as in Equations (3) and (4).  $B_s$  scales as  $I^{1/2} R^{-3} \propto M^{1/2} R^{-2} (1+z)$  (Ravenhall & Pethick 1994), where  $1+z = (1-2GM/Rc^2)^{-1/2} \propto B/E_0$  from Equation (2). For an astrophysically likely  $M = 1.4 M_\odot$ , theoretical NS equations of state allow  $8 \text{ km} < R < 15 \text{ km}$ , therefore  $1.18 < 1+z < 1.44$ . The spectroscopic  $B$  is therefore uncertain by  $\pm 10\%$  when we adopt  $z = 0.3$ , while the dipole  $B_s$  is uncertain by the much larger factor of  $\sim 2$ . (The gravitational redshift cancels out in their ratio.) Allowing for these uncertainties, it is reasonable to adopt the hypothesis that feature(s) in the spectrum of PSR J0821–4300 are due to the cyclotron process.

The continuum X-ray spectrum and pulse profiles of PSR J0821–4300 are indicative of antipodal hot spots of different areas and temperatures (Gotthelf & Halpern 2009; Gotthelf et al. 2010), which are difficult to account for if the magnetic field is weak. A related problem is the high pulsed fraction of 64% from PSR J1852+0040 (Halpern & Gotthelf 2010a), a timing twin of PSR J0821–4300. Polar cap heating by any magnetospheric accelerator must be negligible as a source of surface heating in CCOs, being only a small fraction of the already insignificant spin-down power. Thermal X-rays from residual cooling can be nonuniform if there is anisotropic heat conduction in the star. The effect of different magnetic field configurations on heat transport in the crust and envelope of NSs has been modeled, most recently by Geppert et al. (2004, 2006), Pérez-Azorín et al. (2006a), and Pons et al. (2009). A toroidal field is expected to be the initial configuration generated by differential rotation in the proto-neutron star dynamo (Thompson

& Duncan 1993). One of the effects of crustal toroidal field is to insulate the magnetic equator from heat conduction, resulting in warm spots at the poles. The warm regions can even be of different sizes due to the antisymmetry of the poloidal component of the field (Geppert et al. 2006), which is evocative of the antipodal thermal structure of PSR J0821–4300. To have a significant effect on the heat transport, the crustal toroidal field strength required in these models is  $\sim 10^{15}$  G, many orders of magnitude greater than the poloidal field if the latter is measured by the spin-down. Purely toroidal or poloidal fields are thought to be unstable in an initially fluid NS (Tayler 1973; Flowers & Ruderman 1977), although the toroidal field may be stabilized by a poloidal field that is several orders of magnitude weaker (Braithwaite 2009). We suggest the latter as a viable configuration for a CCO.

Shabaltas & Lai (2012) tried to model the pulse profile of PSR J1852+0040 with anisotropic conduction, and concluded that they needed a toroidal crustal field of  $B_\phi > 2 \times 10^{14}$  G to produce its high pulsed fraction. Even then, they observe, the shape of the modeled light curve does not match the observed one. Since the shape of the light curve is not reproduced, the surface temperature distribution of PSR J1852+0040 and its physical origin are still not known.

Page & Sarmiento (1996), Pérez-Azorín et al. (2006b), Zane & Turolla (2006), and Zane (2007) investigated NS surface emission patterns using a combination of star-centered dipole and quadrupole magnetic field components to model asymmetric pulse profiles. The behavior of PSR J0821–4300 may ultimately be explained by similar models. It remains to be shown whether CCOs can have field configurations that are strong enough to affect heat transport to the extent required, while not exceeding the spin-down limits on the external dipole field.

### 6.3. Origin and Evolution of Anti-magnetars

PSR J0821–4300 is nearly a twin of PSR J1852+0040 in its spin properties, and there are no other young NSs with measured magnetic fields this weak. They fall in a region of the  $P-\dot{P}$  diagram (Figure 3) that is devoid of ordinary (non-recycled) radio pulsars (Manchester et al. 2005). They overlap with the supposed mildly recycled pulsars in this area (Belczynski et al. 2010). The characteristic age of 254 Myr for PSR J0821–4300 is not meaningful because the pulsar was born spinning at its current period, as is the case for the other CCO pulsars. If their magnetic fields remain constant, they will not move in  $P-\dot{P}$  space for  $> 10^8$  yr (but see below). That CCOs are found in SNRs in comparable numbers to other classes of NSs implies that they must represent a significant fraction of NS births. If PSR J0821–4300 and PSR J1852+0040 are typical CCOs, the area around them in the  $P-\dot{P}$  diagram should be densely populated with “orphaned CCOs” that remain after their SNRs dissipate in  $\sim 10^5$  yr. Why there are few ordinary radio pulsars and no older X-ray pulsars near their location is then a mystery, as emphasized by Kaspi (2010), which may indicate that radio luminosity is a function of spin-down power.

There are not yet enough CCOs to know whether they are intrinsically radio-quiet relative to ordinary and recycled pulsars, rather than unfavorably beamed. It is also possible that some ordinary radio pulsars with  $B_s < 10^{11}$  G are actually much younger than their characteristic ages, and may be orphaned CCOs that could be recognized in X-rays. Whether or not they are radio pulsars, nearby orphaned CCOs should

be detectable as thermal X-ray sources for  $10^5$ – $10^6$  yr, similar to the seven *ROSAT*-discovered INSSs (Haberl 2007) which, however, have strong magnetic fields (Kaplan et al. 2009). It is likely that the INSSs are kept hot for longer than CCOs by continuing magnetic field decay (Pons et al. 2007), which would explain their observed abundance relative to the elusive orphaned CCOs. It may be difficult to detect and/or recognize orphaned CCOs if they cool faster than ordinary NSs. One effect that can accelerate cooling is an accreted light-element envelope, which has higher heat conduction than an iron surface (Kaminker et al. 2006). The newly discovered 59 ms pulsar 1RXS J141256.0+792204 (“Calvera”), originally detected in the *ROSAT* All-Sky Survey, may be the first recognized example of an orphaned CCO (Zane et al. 2011; Rutledge et al. 2008; Halpern 2011), pending a measurement of its period derivative. The INSS 2XMM J104608.7–594306 in the Carina Nebula (Pires et al. 2012) has been suggested as another orphaned CCO.

It is possible that the weak magnetic field of CCOs is causally related to slow rotation at birth through the turbulent dynamo (Thompson & Duncan 1993) that generates the magnetic field. (See Spruit 2008 for a review of possible mechanisms for the origin of magnetic fields in NSs.) If the dipole magnetic field  $B_s$  is simply related to the initial spin period, and assuming that the present period  $P$  is in fact the birth period because the spin-down time is so much longer than the true age, we may expect an anti-correlation between  $B_s$  and  $P$ . With only three data points to compare, and with two of them having nearly identical values, there is not much evidence to examine for a trend. In fact, the CCO with the longest period, PSR J1210–5226, also has the strongest dipole field of the three, which would not by itself support such a simple correlation. A population analysis of radio pulsars by Faucher-Giguère & Kaspi (2006) concludes that there is a wide distribution of birth periods, with a mean of  $\sim 300$  ms and a dispersion of  $\sigma \sim 150$  ms. If this is true, the birth periods of CCOs are not in fact long, and their weak dipole fields may be the effect of some as-yet unknown parameter.

In an alternative theory for CCOs, a normal ( $\sim 10^{12}$  G) magnetic field is buried in the core or crust of an NS by prompt fall-back of supernova debris, and takes thousands of years to diffuse back to the surface, during which time the NS appears as an anti-magnetar. This is assuming that the accreted matter is itself not magnetized. The timescale for diffusion is highly dependent on the amount of matter accreted. According to Muslimov & Page (1995), for accretion of  $\sim 10^{-5} M_\odot$ , the regrowth of the surface field is largely complete after  $\sim 10^3$  yr, but if  $> 0.01 M_\odot$  is accreted, then the diffusion time could be millions of years. Chevalier (1989) calculated that the NS in SN 1987A could have accreted  $\sim 0.1 M_\odot$  of fallback material in the hours after the supernova explosion, aided by a reverse shock from the helium layer of the progenitor. If so, it may never emerge as a radio pulsar.

Interesting support for the theory of field burial and regrowth is the absence of evidence for magnetic field strengths  $< 10^{11}$  G in accreting high-mass X-ray binary (HMXB) pulsars, as inferred from their pulse periods and period derivatives (Popov & Turolla 2013). If intrinsic fields in the range  $10^{10}$ – $10^{11}$  G were common, equilibrium spin periods of 0.1–1 s should be frequent in HMXBs, but they are not. If the NSs in these systems are born in the same way as isolated pulsars, this could imply that birth fields are never so small; instead, field regrowth has occurred in all cases after it was initially buried. One caveat here is that  $\sim 40\%$  of HMXBs do not have measured spin periods, although there is no strong selection effect against detecting  $P < 1$  s.

Bernal et al. (2010) has revisited the process of hypercritical accretion onto a magnetized NS, while Ho (2011) made new calculations of the subsequent diffusion to constrain the magnetic fields of CCOs at birth and the accreted mass, finding  $10^{-4}$  to  $10^{-5} M_{\odot}$  for the latter. These models are difficult to test using CCOs because it would involve measuring the braking index or the change of the dipole magnetic field directly. Ho (2011) implied that the isolation of CCOs in the  $P-\dot{P}$  diagram may be less problematic in this model because, as their dipole magnetic fields increase, they will evolve to join the bulk of the pulsar population. However, for the first  $\sim 10^5$  yr, field growth can only move a CCO vertically upward in the  $P-\dot{P}$  diagram, as the braking index has a large, negative value. Orphaned CCOs should still have periods of  $\sim 0.1$  s and lie in a sparse region. For this reason, an important test for an example of field growth is to determine the  $\dot{P}$  of Calvera, which will reveal whether its dipole field is greater than that of PSR J0821–4300 and PSR J1852 + 0040.

Previous calculations of field burial and re-emergence for CCOs were one dimensional. The first two-dimensional calculations for this purpose were recently reported by Viganò & Pons (2012). They find that the accretion must be essentially isotropic to bury the field sufficiently to cause the required orders-of-magnitude reduction of the external dipole. If the accretion were instead confined to the equator or the magnetic poles, the reduction of the dipole component would not be significant enough to produce a CCO. Finally, it remains to be seen whether the resulting surface thermal distribution during the CCO phase can be made compatible with observed spectra and pulse profiles. Viganò & Pons (2012) briefly presented the temperature distribution from one of their models that produces hot polar caps at a time when the external dipole field is  $10^{10}$  G. But even in this case, the temperature does not vary by as much as a factor of two over the surface, a range that would be required to match the properties of PSR J0821–4300 and other CCOs.

## 7. CONCLUSIONS AND FUTURE WORK

Measurement of the spin-down rate of the 112 ms PSR J0821–4300 in Puppis A was achieved using X-ray observations coordinated between *XMM-Newton* and *Chandra*, the resulting phase-connected ephemeris spanning 2.3 yr. We also measured the proper motion of the pulsar in *Chandra* HRC images over 10.6 yr. The proper motion makes a non-negligible contribution to the period derivative via the Shklovskii effect, and the uncertainty in proper motion and distance limits the accuracy of the intrinsic period derivative to  $\approx 16\%$ . The straightforward interpretation of these results is dipole spin-down due to a weak surface magnetic field of  $B_s = 2.9 \times 10^{10}$  G, the smallest measured for any young NS, and nearly identical to that of the CCO pulsar PSR J1852 + 0040 in Kes 79.

A phase-dependent spectral feature in PSR J0821–4300 can be modeled either as an emission line of energy  $\approx 0.75$  keV, or as a cyclotron absorption line and its harmonic, with  $E_0 \approx 0.46$  keV. For reasons that are not clear, it is stronger during the pulse-phase interval in which the continuum spectrum is softer. There is only marginal evidence for long-term variability of this feature. The local magnetic field strength in the area where the spectral feature is produced may have to be larger than the dipole spin-down value.

The existing spin-down measurements for three CCOs, including a definitive new result for PSR J1210–5226, are compelling evidence that a weak dipole field component is the physical origin of the CCO class in general. It is reasonable

to assume that the CCOs that have not yet been seen to pulse have magnetic fields that are similar to or weaker than those of PSR J0821–4300 and PSR J1852 + 0040. Otherwise, if their fields were stronger, their spectra should show cyclotron lines similar to PSR J1210–5226 and (possibly) PSR J0821–4300. Deep X-ray timing searches of the remaining members of this class, to smaller limits on pulsed fraction, could still discover new pulsars and supply valuable data on their birth properties and evolution.

A remaining theoretical puzzle about CCOs is the origin of their surface temperature anisotropies, in particular, the one or two warm/hot regions that are smaller than the full NS surface. The measured spin-down power is too small to contribute to this emission. Continuing accretion is unlikely because of the small spin-down rates. It appears that any explanation will have to involve stronger magnetic field components in the crust, with toroidal or quadrupolar geometries, that do not contribute to the dipole spin-down torque. A physical model of thermal and magnetic field structure that self-consistently reproduces the spin-down rates, X-ray spectra, and pulse profiles is still needed. If it can be studied with better data, the details of the phase-dependent and possibly variable spectral feature from PSR J0821–4300 may contribute to a more definite model of its surface magnetic field geometry.

The CCO pulsars PSR J1852 + 0040 and PSR J0821–4300 fall in a region of  $B-P$  space that overlaps with what are assumed to be moderately recycled pulsars, but is otherwise empty. An understanding of the evolutionary status of CCOs is critically dependent upon a search for their descendants, the orphaned CCOs without SNRs. Some single radio pulsars with spin parameters similar to CCOs may be orphaned CCOs rather than recycled pulsars, and they may be much younger than their characteristic ages. X-ray observations of pulsars in this region may find evidence of their relative youth via surface thermal emission. The spin-down rates of orphaned CCOs would reveal whether CCOs have intrinsically weak magnetic fields, or whether field re-emerges on a timescale of  $\sim 10^4$  yr from a normal magnetic field that was buried by prompt fallback of supernova debris, as is invoked in some theoretical studies. Such rapid evolution would lead to orphaned CCOs that lie directly above CCOs on the  $P-\dot{P}$  diagram but are still detectable as thermal X-ray sources. The radio-quiet pulsar Calvera is a possible such candidate. Whether or not CCOs have buried fields, the paucity of radio pulsars with similar spin parameters is real and requires an explanation.

We thank Dany Page, and the anonymous referee, for helpful comments. This investigation is based on observations obtained with *XMM-Newton*, an ESA science mission with instruments and contributions directly funded by ESA Member States and NASA, and *Chandra*. The opportunity to propose joint, coordinated observations between *XMM-Newton* and *Chandra* was crucial for the success of this effort. Financial support was provided by NASA grants NNX11AD19G and NNX12AD41G for the *XMM-Newton* observations, and by *Chandra* awards GO1-12001X and SAO GO1-12071X, issued by the Chandra X-ray Observatory Center, which is operated by the Smithsonian Astrophysical Observatory for and on behalf of NASA under contract NAS8-03060.

## REFERENCES

- Abramowski, A., Acero, F., Aharonian, F., et al. 2011, *A&A*, 531, 81  
Bamba, A., Yamazaki, R., & Hiraga, J. S. 2005, *ApJ*, 632, 294

- Becker, W., Prinz, T., Winkler, P. F., & Petre, R. 2012, *ApJ*, **755**, 141
- Belczynski, K., Lorimer, D. R., Ridley, J. P., & Curran, S. J. 2010, *MNRAS*, **407**, 1245
- Bernal, C. G., Lee, W. H., & Page, D. 2010, *RMxAA*, **46**, 309
- Bhattacharya, D., Wijers, R. A. M. J., Hartman, J. W., & Verbunt, F. 1992, *A&A*, **254**, 198
- Bignami, G. F., Caraveo, P. A., De Luca, A., & Mereghetti, S. 2003, *Natur*, **423**, 725
- Braithwaite, J. 2009, *MNRAS*, **397**, 763
- Buccheri, R., Bennett, K., Bignami, G. F., et al. 1983, *A&A*, **128**, 245
- Cassam-Chenai, G., Decourchelle, A., Ballet, J., et al. 2004, *A&A*, **427**, 199
- Castelletti, G., Dubner, G., Golap, K., & Goss, W. M. 2006, *A&A*, **459**, 535
- Chakrabarty, D., Pivovaroff, M. J., Hernquist, L. E., Heyl, J. S., & Narayan, R. 2001, *ApJ*, **548**, 800
- Chevalier, R. A. 1989, *ApJ*, **346**, 847
- De Luca, A. 2008, in AIP Conf. Ser. 983, 40 Years of Pulsars: Millisecond Pulsars, Magnetars, and More, ed. C. Bassa et al. (Melville, NY: AIP), 311
- De Luca, A., Mereghetti, S., Caraveo, P. A., et al. 2004, *A&A*, **418**, 625
- De Luca, A., Mignani, R. P., Sartori, A., et al. 2011, *A&A*, **525**, A106
- De Luca, A., Salvetti, D., Sartori, A., et al. 2012, *MNRAS*, **421**, L72
- Faucher-Giguère, C.-A., & Kaspi, V. M. 2006, *ApJ*, **643**, 332
- Fesen, R. A., Hammell, M. C., Morse, J., et al. 2006, *ApJ*, **645**, 283
- Flowers, E., & Ruderman, M. A. 1977, *ApJ*, **215**, 302
- Gaensler, B. M., Tanna, A., Slane, P. O., et al. 2008, *ApJL*, **680**, L37
- Geppert, U., Küker, M., & Page, D. 2004, *A&A*, **426**, 267
- Geppert, U., Küker, M., & Page, D. 2006, *A&A*, **457**, 937
- Gotthelf, E. V., & Halpern, J. P. 2007, *ApJL*, **664**, L35
- Gotthelf, E. V., & Halpern, J. P. 2009, *ApJL*, **695**, L35
- Gotthelf, E. V., Halpern, J. P., & Seward, F. D. 2005, *ApJ*, **627**, 390
- Gotthelf, E. V., Perna, R., & Halpern, J. P. 2010, *ApJ*, **724**, 1316
- Haberl, F. 2007, *Ap&SS*, **308**, 181
- Halpern, J. P. 2011, *ApJL*, **736**, L3
- Halpern, J. P., & Gotthelf, E. V. 2010a, *ApJ*, **709**, 436
- Halpern, J. P., & Gotthelf, E. V. 2010b, *ApJ*, **710**, 941
- Halpern, J. P., & Gotthelf, E. V. 2010c, *ApJ*, **725**, 1384
- Halpern, J. P., & Gotthelf, E. V. 2011, *ApJL*, **733**, L28
- Halpern, J. P., Gotthelf, E. V., Camilo, F., & Seward, F. D. 2007, *ApJ*, **665**, 1304
- Heinke, C. O., & Ho, W. C. G. 2010, *ApJL*, **719**, L167
- Ho, W. C. G. 2011, *MNRAS*, **414**, 2567
- Ho, W. C. G., & Heinkel, C. O. 2009, *Natur*, **462**, 71
- Hobbs, G., Lorimer, D. R., Lyne, A. G., & Kramer, M. 2005, *MNRAS*, **360**, 974
- Hui, C. Y., & Becker, W. 2006a, *A&A*, **454**, 543
- Hui, C. Y., & Becker, W. 2006b, *A&A*, **457**, L33
- Iyudin, A. F., Aschenbach, B., Becker, W., Dennerl, K., & Haberl, F. 2005, *A&A*, **429**, 225
- Kaminker, A. D., Gusakov, M. E., Yakovlev, D. G., & Gnedin, O. Y. 2006, *MNRAS*, **365**, 1300
- Kaplan, D. L., & van Kerkwijk, M. H. 2009, *ApJ*, **705**, 798
- Kargaltsev, O., Pavlov, G. G., Sanwal, D., & Garmire, G. P. 2002, *ApJ*, **580**, 1060
- Kaspi, V. M. 2010, *PNAS*, **107**, 7147
- Katsuda, K., Tsunemi, H., Mori, K., et al. 2012, *ApJ*, **756**, 49
- Lazendic, J. S., Slane, P. O., Gaensler, B. M., et al. 2003, *ApJL*, **593**, L27
- Leahy, D. A., Elsner, R. F., & Weisskopf, M. C. 1983, *ApJ*, **272**, 256
- Lovchinsky, I., Slane, P., Gaensler, B. M., et al. 2011, *ApJ*, **731**, 70
- Makishima, K., Miura, T., Ishida, M., et al. 1990, *ApJL*, **365**, L59
- Manchester, R. N., Hobbs, G. B., Teoh, A., & Hobbs, M. 2005, *AJ*, **129**, 1993
- Mereghetti, S., De Luca, A., Caraveo, P. A., et al. 2002a, *ApJ*, **581**, 1280
- Mereghetti, S., Tiengo, A., & Israel, G. L. 2002b, *ApJ*, **569**, 275
- Mihara, T., Makishima, K., Ohashi, T., Sakao, T., & Tashiro, M. 1990, *Natur*, **346**, 250
- Muslimov, A., & Page, D. 1995, *ApJL*, **400**, L77
- Page, D., Prakash, M., Lattimer, J. M., & Steiner, A. W. 2011, *PhRvL*, **106**, 081101
- Page, D., & Sarmiento, A. 1996, *ApJ*, **473**, 1067
- Park, S., Kargaltsev, O., Pavlov, G. G., et al. 2009, *ApJ*, **695**, 431
- Park, S., Mori, K., Kargaltsev, O., et al. 2006, *ApJL*, **653**, L37
- Pavlov, G. G., & Luna, G. J. M. 2009, *ApJ*, **703**, 910
- Pavlov, G. G., Zavlin, V. E., Aschenbach, B., Trümper, J., & Sanwal, D. 2000, *ApJL*, **531**, L53
- Pérez-Azorín, J. F., Miralles, J. A., & Pons, J. A. 2006a, *A&A*, **451**, 1009
- Pérez-Azorín, J. F., Pons, J. A., Miralles, J. A., & Miniutti, G. 2006b, *A&A*, **459**, 175
- Pires, A. M., Motch, C., Turolla, R., et al. 2012, *A&A*, **544**, A17
- Pons, J. A., Link, B., Miralles, J. A., & Geppert, U. 2007, *PhRvL*, **98**, 071101
- Pons, J. A., Miralles, J. A., & Geppert, U. 2009, *A&A*, **496**, 207
- Popov, S. B., & Turolla, R. 2013, in ASP Conf. Ser. 466, Electromagnetic Radiation from Pulsars and Magnetars, ed. W. Lewandowski (San Francisco, CA: ASP), 191
- Ravenhall, D. G., & Pethick, C. J. 1994, *ApJ*, **424**, 846
- Reynolds, S. P., Borkowski, K. J., Hwang, U., et al. 2006, *ApJL*, **652**, L45
- Reynoso, E. M., Dubner, G. M., Gross, W. M., & Arnal, E. M. 1995, *AJ*, **110**, 318
- Reynoso, E. M., Green, A. J., Johnston, S., et al. 2003, *MNRAS*, **345**, 671
- Rutledge, R. E., Fox, D. B., & Shevchuk, A. H. 2008, *ApJ*, **672**, 1137
- Sánchez-Ayaso, E., Combi, J. A., Albacete Colombi, J. F., et al. 2012, *A&AS*, **337**, 573
- Sanwal, D., Pavlov, G. G., Zavlin, V. E., & Teter, M. A. 2002, *ApJ*, **574**, 61
- Seward, F. D., Slane, P. O., Smith, R. K., & Sun, M. 2003, *ApJ*, **584**, 414
- Shabaltas, N., & Lai, D. 2012, *ApJ*, **748**, 148
- Shklovskii, I. S. 1970, *SvA*, **13**, 562
- Shternin, P. S., Yakovlev, D. G., Heinke, C. O., Ho, W. C. G., & Patnaude, D. J. 2011, *MNRAS*, **412**, L108
- Slane, P., Hughes, J. P., Edgar, R. J., et al. 2001, *ApJ*, **548**, 814
- Spitkovsky, A. 2006, *ApJL*, **648**, L51
- Spruit, H. C. 2008, in AIP Conf. Ser. 983, 40 Years of Pulsars: Millisecond Pulsars, Magnetars, and More, ed. C. Bassa et al. (Melville, NY: AIP), 391
- Strutt, J. W. 1880, *PMag*, 10, 73
- Suleimanov, V. E., Pavlov, G. G., & Werner, K. 2010, *ApJ*, **714**, 635
- Suleimanov, V. E., Pavlov, G. G., & Werner, K. 2012, *ApJ*, **751**, 15
- Tayler, R. J. 1973, *MNRAS*, **161**, 365
- Thompson, C., & Duncan, R. C. 1993, *ApJ*, **408**, 194
- Thorstensen, J. R., Fesen, R. A., & van den Bergh, S. 2001, *AJ*, **122**, 297
- Tian, W. W., Leahy, D. A., Havercorn, M., & Jiang, B. 2008, *ApJL*, **679**, L85
- van den Heuvel, E. P. J. 1987, in IAU Symp. 125, The Origin and Evolution of Neutron Stars, ed. D. J. Helfand & J. Huang (Dordrecht: Reidel), 393
- Viganò, D., & Pons, J. A. 2012, *MNRAS*, **425**, 2487
- Winkler, P. F., & Petre, R. 2007, *ApJ*, **670**, 635
- Winkler, P. F., Tuttle, J. H., Kirshner, R. P., & Irwin, M. J. 1988, in IAU Colloq. 101, Supernova Remnants and the Interstellar Medium, ed. R. S. Roger & T. L. Landecker (Cambridge: Cambridge Univ. Press), 65
- Woermann, B., Gaylard, M. J., & Otrupcek, R. 2000, *MNRAS*, **317**, 421
- Zacharias, N., Finch, C., Girard, T., et al. 2010, *AJ*, **139**, 2184
- Zane, S. 2007, *Ap&SS*, **308**, 259
- Zane, S., Haberl, F., Israel, G. L., et al. 2011, *MNRAS*, **410**, 2428
- Zane, S., & Turolla, R. 2006, *MNRAS*, **366**, 727
- Zavlin, V. E., Pavlov, G. G., Sanwal, D., & Trümper, J. 2000, *ApJL*, **540**, L25